JGR Space Physics

RESEARCH ARTICLE
10.1029/2022JA031074

Nighttime Midlatitude E-F Coupling in Geomagnetic Conjugate Ionospheres: A Double Thin Shell Model and a Multi-Source Data Investigation

Weizheng Fu[1], Tatsuhiro Yokoyama[1], Nicholas Ssessanga[2], Guanyi Ma[3], and Mamoru Yamamoto[1]

[1]Research Institute for Sustainable Humanosphere, Kyoto University, Kyoto, Japan, [2]Department of Physics, 4DSpace, University of Oslo, Oslo, Norway, [3]National Astronomical Observatories, Chinese Academy of Sciences, Beijing, China

Key Points:

- The F-region geomagnetic conjugate medium-scale traveling ionospheric disturbances (MSTIDs) in both hemispheres are mainly driven by the Es layers in the summer hemisphere
- Preexisting Es layers in the winter hemisphere show intensity reduction or even dissipation after the interhemispheric coupling
- The amplitude and growth rate of hemispheric conjugate MSTIDs are smaller in the winter hemisphere

Correspondence to:
W. Fu,
fu.weizheng.40y@st.kyoto-u.ac.jp

Citation:
Fu, W., Yokoyama, T., Ssessanga, N., Ma, G., & Yamamoto, M. (2023). Nighttime midlatitude E-F coupling in geomagnetic conjugate ionospheres: A double thin shell model and a multi-source data investigation. *Journal of Geophysical Research: Space Physics*, *128*, e2022JA031074. https://doi.org/10.1029/2022JA031074

Received 8 OCT 2022
Accepted 4 MAR 2023

Author Contributions:
Conceptualization: Weizheng Fu, Tatsuhiro Yokoyama, Guanyi Ma
Formal analysis: Weizheng Fu, Nicholas Ssessanga
Investigation: Weizheng Fu, Tatsuhiro Yokoyama
Methodology: Weizheng Fu, Nicholas Ssessanga
Project Administration: Mamoru Yamamoto
Software: Weizheng Fu
Supervision: Tatsuhiro Yokoyama, Mamoru Yamamoto
Validation: Weizheng Fu, Tatsuhiro Yokoyama
Visualization: Weizheng Fu

Abstract Geomagnetic conjugate mid-latitude nighttime ionospheres are frequently simultaneously populated with electrified nighttime medium-scale traveling ionospheric disturbances (MSTIDs). Earlier observations and theoretical analysis have underscored the ionosphere E-F coupling and the postulation of coupled conjugate hemispheres, playing a pivotal role in the formation of electrified MSTIDs. In this paper, the conjugate MSTIDs are studied to elucidate the causes and effects of E-F coupling in the interhemispheric coupled ionosphere. The hemisphere-coupled ionospheres over Japan and Australia are observed and analyzed using total electron content (TEC) measurements, supplemented with multi-source observations from ionosondes, Ionospheric Connection Explorer (neutral wind), Constellation Observing System for Meteorology, Ionosphere, and Climate (electron density), and Swarm (magnetic field). A double-thin-shell model is introduced to analyze the ionospheric responses in E and F regions during the coupling process. For the first time, observation results provide the evidence that F-region geomagnetic conjugate irregularities in both hemispheres are mainly driven by the Es layers in the summer hemisphere. The Es layer in the summer hemisphere subsequently triggers local E-F coupling and inter-hemispheric coupling. In the winter hemisphere, Es layers show amplitude reduction or even dissipation during the interhemispheric coupling process. Furthermore, thermospheric winds, non-equipotential magnetic field lines, and background TEC are presumed candidates for the inter-hemispheric asymmetry in MSTIDs amplitudes and growth rates.

1. Introduction

Electrified ionosphere irregularities have extensively been an intriguing subject of research. In the summer hemisphere, at mid-latitudes during nighttime, electrified irregularities are ubiquitous in the F-region, manifested as wave-like electron density perturbations with horizontal wavelengths of several hundred kilometres and periods of 15–60 min (Bowman, 1985, 1990; Hunsucker, 1982): typically known as medium-scale traveling ionospheric disturbances (MSTIDs). Recent studies have identified the characteristics of MSTIDs by using two-dimensional (2D) GPS-TEC (total electron content) maps (A. Saito, Fukao, & Miyazaki, 1998), three-dimensional (3-D) computerized ionospheric tomography technique (Ssessanga et al., 2015), and airglow imagers (Shiokawa, Ihara, et al., 2003). One of the intriguing aspects of nighttime midlatitude MSTIDs is the northwest-southeast (NW-SE) (northeast-southwest; NE-SW) aligned frontal structures propagating toward equator-westward direction in the Northern (Southern) Hemisphere (Yokoyama, 2014). The Perkins instability could be the most likely mechanism to account for the directional preference of alignment and propagation of MSTID structures (Perkins, 1973). However, theoretical analysis have found that the growth rates of typical MSTIDs cannot be satisfied by a standalone Perkins instability, and have underscored a coupled effect from polarized Es structures (Es-layer instability) coupled to the Perkins instability (Cosgrove & Tsunoda, 2002, 2004; Cosgrove et al., 2004; Tsunoda & Cosgrove, 2001; Yokoyama et al., 2009).

Es (sporadic E) are thin layers of metallic ion plasma that predominantly form at altitudes of 95–125 km in the ionospheric E region (Whitehead, 1989). Occasionally, the Es layer anomalously exhibits greater plasma densities than the F region; an occurrence that highly correlates with intense trans-ionospheric signal scintillation (Fu, Ssessanga, et al., 2021). For Es layers at midlatitudes, neutral wind shear theory has been widely accepted for the generation mechanism (Haldoupis, 2012; Mathews, 1998), and the pronounced seasonal dependence is attributed to the tidal wind, the Earth's geomagnetic field, and the level of meteoric depositions (Haldoupis et al., 2007; Whitehead, 1989). Albeit the Es horizontal structures (~100 km in length and 10 km in width (Maeda

Writing – original draft: Weizheng Fu
Writing – review & editing: Weizheng Fu, Tatsuhiro Yokoyama, Nicholas Ssessanga, Guanyi Ma, Mamoru Yamamoto

& Heki, 2015; Sinno et al., 1964)) is smaller when compared to MSTIDs, simulation studies have found the former to play an important role in the generation of nighttime midlatitude MSTIDs via electromagnetic coupling along the geomagnetic field lines (Yokoyama & Hysell, 2010; Yokoyama et al., 2009). Indeed, in the Northern Hemisphere summer nights, observation results show that during the coupling process, Es layers and MSTIDs share common alignment (NW-SE), propagation phase velocity (about 100 m/s), direction (southwestward; SW), and density perturbations traced along a common geomagnetic field line (Fu et al., 2022; Liu et al., 2019; S. Saito et al., 2007). Still under simulation analysis, a weak electric field polarization from MSTIDs could map down to the E region, thus seeding the Es-layer instability and producing additive polarization fields that amplify the Perkins instability in the F region (Cosgrove, 2007).

Actually, the E-F coupling process is more intricate, to the extent that MSTIDs are simultaneously observed in the geomagnetic conjugate regions (different hemispheres) with matching crests and troughs (Narayanan et al., 2018; Otsuka et al., 2004; Shiokawa et al., 2005; Valladares & Sheehan, 2016). Simulation works have verified that these geomagnetic conjugate structures are the results of interhemispheric coupling (Yokoyama, 2014). In this process, the polarization electric fields generated by E- and F-region irregularities can be mapped to opposite hemisphere along the geomagnetic field lines with a certain attenuation, which can well explain the maximum and secondary occurrence peak of MSTIDs in summer and winter in the statistic study of Shiokawa, Ihara, et al. (2003). Otsuka et al. (2008) suggested that Es layers in the summer hemisphere could be important for the generation of MSTIDs in both hemispheres. Narayanan et al. (2018) analyzed the simultaneous MSTID structures in geomagnetic conjugate regions by using all-sky airglow imagers and ionosondes. They found that the Es layers and thermospheric meridional winds play a major role in the interhemispheric MSTIDs. By using the long-term radio occultation observations, Liu et al. (2020) inferred that the MSTIDs are closely related to the effect of E-F coupling and interhemispheric coupling; Lee et al. (2021) found that the MSTID generation is also affected by some factors other than Es, for example, the growth rate of the Perkins instability, atmospheric gravity waves (AGWs), and the F-region conductance. Due to the limited observation area, resolution, and methods, comparing the temporal relationship between the occurrence of Es and MSTIDs is difficult, and thus the causal relationship in the E-F and interhemispheric coupling is not yet fully understood. Therefore, a comprehensive analysis of the interhemispheric coupled ionosphere is required to deepen our understanding of MSTIDs.

In response to the above problems, we attempt at simultaneously analyzing the geomagnetic conjugate structures at a broader horizontal scale and higher temporal resolution. Global navigation satellite systems (GNSSs) have been widely utilized for ionospheric studies because of its cost-effectiveness and rapid development. A densely distributed network of ground-based receivers, from regional to global, enables us to monitor the ionosphere and probe the ionospheric disturbances with a higher spatiotemporal resolution (Ding et al., 2011; Otsuka et al., 2013). This paper mainly focuses on the conjugate regions in Japan and Australia since both Es and MSTIDs have been frequently observed in the East Asian sector (Kil & Paxton, 2017; Wu et al., 2005). We observe the ionospheric disturbances in geomagnetic conjugate regions with ground-based GNSS TEC. A double-thin-shell approach is introduced to analyze the ionospheric E- and F-region responses during the coupling process. Additionally, to help clarify and verify the causes and effects of E-F coupling process in the interhemispheric coupled ionosphere, the conjugate E and F regions of both the hemispheres are studied with multi-source observations, including GNSS TEC, ionosondes, radio occultation, Swarm satellite constellation, and Ionospheric Connection Explorer (ICON) spacecraft. The data and methods used in this analysis are presented in Section 2. Observation results and discussion are shown in Section 3 and Section 4, respectively. Section 5 gives the final conclusions.

2. Data and Methods

This study focuses on mid-latitude geomagnetic conjugate regions found in Japan and Australia. Figure 1a shows the distribution of ground-based GNSS receivers and ionosondes in these areas. Gray dashed lines represent the magnetic dip (0°, ±20°, and ±50°) calculated from International Geomagnetic Reference Field (IGRF) model (Alken et al., 2021). Compared to the dense GNSS Earth Observation Network (GEONET) over Japan, with more than 1,000 receivers, the network over Australia consists of approximately 450 sparsely distributed stations with a bias toward the southeast. For a 30 s data cadence, more than 5,000 (1,800) ray paths are recorded over Japan (Australia) with a cutoff elevation angle of 35° (A. Saito, Fukao, & Miyazaki, 1998). Figures 1b and 1c show an example of ionospheric pierce points (IPPs) from GNSS rays. The epoch is arbitrarily selected, and the altitude is 300 km. The disparity in the distribution of the IPP points follows that of the two networks. Because the Japanese

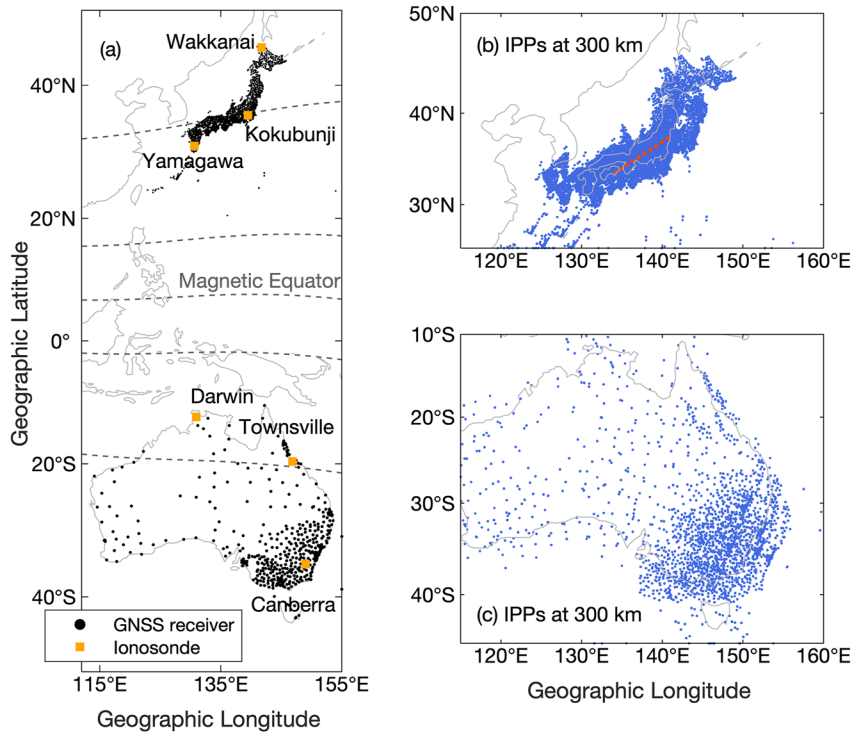

Figure 1. (a) Distribution of global navigation satellite systems (GNSS) stations (black dots) and ionosondes (yellow squares). Gray dashed lines represent the magnetic dip (0°, ±20°, ±50°). (b and c) Blue dots represent the distribution of ionospheric pierce point (IPP) at 10:00 UT (universal time) on 29 July 2019, at 300 km altitude. Red dashed line indicates the region with most data points over Japan.

archipelago is narrow and vividly stretches northeast to southwest, the red dashed line in Figure 1b indicates the region with the most data points where reconstructions are of better accuracy.

Slant TEC (STEC) is the integrated electron density along the line of sight (LOS) between the receiver and satellite. Usually, the TEC in ionospheric studies refer to the vertical TEC, which can be obtained from a STEC and a mapping function under the single-thin-shell model. This model assumes an infinitesimally thin layer at a constant height represents the whole ionosphere. Although the single-thin-shell model has been widely applied in ionospheric studies, its exploitation in E-F coupling is difficult because of the impossibility of observing perturbations in both E and F regions. Fu et al. (2022) simultaneously reconstructed the E- and F-region disturbances over Japan by using the dense ground-based GNSS TEC and a double-thin-shell approach, which has proven to be an effective tool to analyze the E-F coupling. However, currently this technique is applicable only over Japan area due to the high spatial density (15–25 km of typical horizontal separations) of GEONET. Therefore, we applied the single- and double-thin-shell approaches to reconstruct the E- and F-region disturbances over Japan, while in the Australian region we only used the single-thin-shell approach to monitor and analyze the irregularity structures in the F region. Additionally, although many receivers started tracking other GNSS satellite constellations, we only focus on GPS in this research because data points are dense enough and the results would not be significantly different if signals from other constellations are included. The STEC were derived from pseudo-range and phase measurements, and the unknown ambiguities in the phase measurements were corrected by the corresponding pseudo-range measurements (Ma et al., 2014; A. Saito, Fukao, & Miyazaki, 1998). We assumed the instrumental biases inherent in satellites and receivers remain stable within one UT (universal time) day (Ma & Maruyama, 2003). STEC with elevation angles smaller than 35° were negated to mitigate the multipath effects. Following the work of Fu et al. (2022), we ingested the TEC perturbation (TECP) component, since typical TECPs caused by Es and MSTIDs are small and the accuracy of absolute GNSS TEC estimation is a few TEC units (TECU; 1 TECU = 10^{16} el/m^2). Similarly, in this paper, TECPs were obtained after deducting a 30-min data running average (centered on the epoch of the LOS) from each LOS TEC, and data corresponding to arc segments less than 30 min were excluded to avoid spurious perturbations.

Ionosondes are one of the most accurate tools for probing the ionosphere. Yellow squares in Figure 1a show the distribution of ionosondes used in this study, located at Wakkanai (45.16°N, 141.75°E geographic; 59.89° magnetic dip, calculated from IGRF model), Kokubunji (35.71°N, 139.49°E geographic; 49.67° magnetic dip), Yamagawa (31.20°N, 130.62°E geographic; 45.38° magnetic dip), Canberra (35.32°S, 149.00°E geographic; −65.96° magnetic dip), Townsville (19.63°S, 146.85°E geographic; −48.87° magnetic dip), and Darwin (12.45°S, 130.95°E geographic; −39.48° magnetic dip). We adapted ionogram observations to indicate the variation of Es-layer intensity at those ionosonde locations. The Es information (critical (foEs) and blanketing (fbEs) frequencies) over Japan and Australia are provided by the manual-scaled (at 1-hr interval) and auto-scaled (at 5-min interval) ionogram parameters, respectively, since the ionogram automatic processing algorithm in Japan cannot detect small fbEs values. On an ionogram, foEs indicates the maximum frequency of the Es echo trace, while fbEs denotes the minimum frequency of the F-layer trace (Narayanan et al., 2018). foEs and fbEs determine the frequency bands in which radio waves can be partially reflected or pass through the Es layer (Maruyama et al., 2006), where fbEs is the peak density of the quasi-uniform layer (i.e., signals lower than this frequency cannot pass through this layer), and foEs is the peak density of clumps within this layer. Thus, the difference between foEs and fbEs (foEs-fbEs) is often used to represent the degree of density structuring in the Es layer (Otsuka et al., 2008).

Spaceborne GNSS radio occultation of Constellation Observing System for Meteorology, Ionosphere, and Climate (COSMIC) have advantages of high accuracy and vertical resolution, which can complement the ground-based GNSS observations with its global coverage (Fu, Ma, et al., 2021). Six satellites in COSMIC-2 mission were operational after 25 June 2019, providing uniform global data coverage with several thousand electron density profiles daily, especially near the equatorial region (Cherniak et al., 2021). The electron density profiles are generated from TEC measurements along the spaceborne receiver and GNSS satellite link by using the Abel inversion technique and local spherical symmetry assumption (Lin et al., 2020). We use these profiles to complement the sparse ground-based observations over Australia: the data used are a level-2 product (ionPrf) from COSMIC-2 with an acceptable degree of uncertainty.

The Swarm mission comprises a constellation of three satellites, in polar orbits at two different altitudes of ≤460 km for Alpha (A) and Charlie (C), and ≤530 km for Bravo (B). Each satellite has an Absolute Scalar Magnetometer and a Vector Fluxgate Magnetometer for measuring Earth's magnetic field at 1 Hz resolution, and a Langmuir Probe for measuring situ electron densities at a 2 Hz resolution (Olsen et al., 2015). In this work, we used the level-1b products of electron density and magnetic field from satellites A and C because they are at the same orbital altitude.

The Michelson Interferometer for Global High-resolution Thermospheric Imaging (MIGHTI) on the ICON spacecraft provides neutral wind data from 90 to 300 km altitude by using 557.7 nm (green channel) and 630.0 nm (red channel) airglow emission observations. More details on instruments and data validation can be found at Makela et al. (2021) and Harding et al. (2021). Following the work of Harding et al. (2022), above and below 180 km, we used the neutral wind data from red channel and green channel, respectively.

3. Observation Results

Earlier statistical studies on nighttime midlatitude MSTIDs in Japanese and Australian longitudinal sector found the occurrence rate to peak in summer, followed by winter (Shiokawa, Ihara, et al., 2003). In this study, due to the limitations of date coverage of multi-source data, a quick look into the summer period, two nighttime MSTID events of similar amplitudes in July (summer in the Northern Hemisphere) and December (summer in the Southern Hemisphere), 2019, were selected for analysis. To mitigate anomalies due to external forcings such as geomagnetic storms, the selected events are from quiet days with $K < 4$ and $|Dst| < 30$ (Ma et al., 2014). The K index is provided by Kakioka magnetic observatory at 36.2°N, 140.2°E.

3.1. Event on 29 July 2019

Figure 2 shows the snapshots of TECP maps at various time epochs from 10:00 to 14:00 UT on 29 July 2019 (DOY (day of year) 210), which are obtained by using the single-thin-shell approach at 300 km altitude, following the method in Tsugawa et al. (2018). Following the difference in the distribution of the ground GNSS receivers, the horizontal spatial resolution of the images in the Northern (Japan) and Southern (Australia) hemispheres

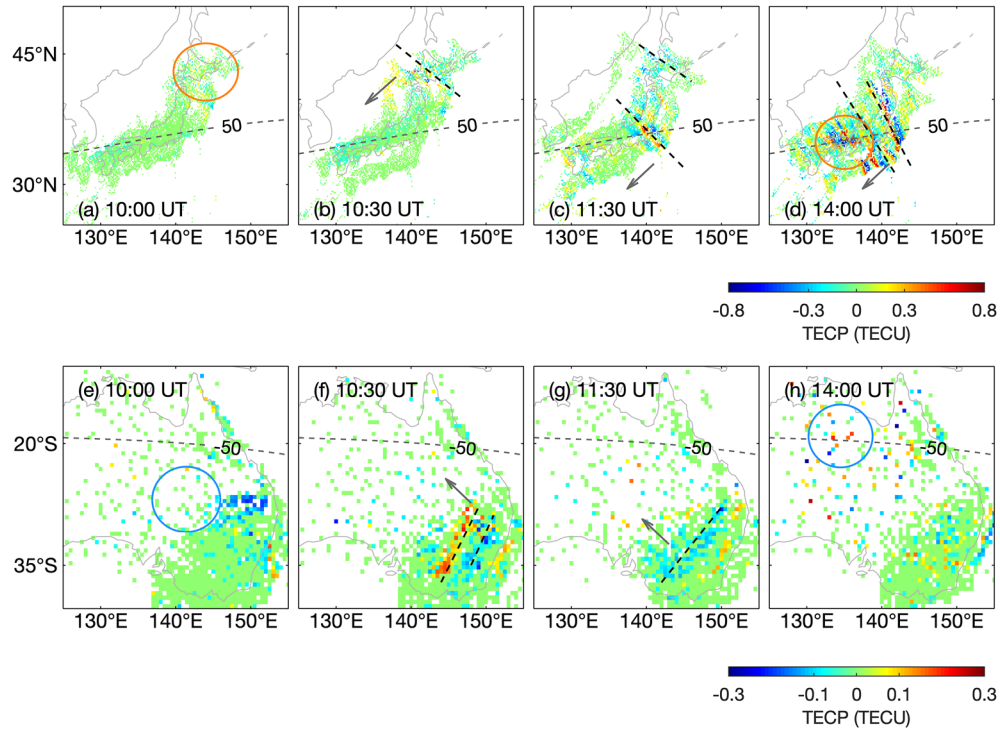

Figure 2. Snapshots of total electron content perturbation (TECP) maps at various time epochs from 10:00 to 14:00 UT (universal time) on 29 July 2019 (DOY (day of year) 210), obtained by the single-thin-shell approach at 300 km altitude. Gray dashed lines represent the magnetic dip at ±50°, orange and blue circles indicate the geomagnetic conjugate regions over Japan (summer) and Australia (winter), black dashed lines indicate the alignment azimuths of the apparent frontal structures, and gray arrows denote the drift direction.

is 0.15° and 0.5°, respectively. In each image, reconstructions are from perturbations collected over a 2-min window: that is, the ionosphere is assumed stationary within this window. Gray dashed lines represent the magnetic dip at ±50° obtained from IGRF model, orange and blue circles indicate the geomagnetic conjugate regions over Japan (summer) and Australia (winter), the black dashed lines drawn along the disturbances indicate the alignment azimuths of the apparent frontal structures, which are NW-SE (NE-SW) in the Northern (Southern) Hemisphere, and gray arrows denote the southwestward (northwestward) drift direction in the Northern (Southern) Hemisphere.

In Figure 2a, in the region circled by the orange line, irregular ionospheric density perturbations (maximum value: 0.34 TECU) are observed over the Japan Archipelago after sunset at 10:00 UT (19:00 JST (Japan standard time)) at higher latitudes (>43°N). Meanwhile (10:00 UT; 20:00 AEST (Australia Eastern Standard Time)), as shown in subplot (e), east-west (E-W) aligned density depletions and irregular perturbations with small amplitudes (<0.17 TECU) are observed in the eastern part of the blue circle, about less than half of those in the summer hemisphere (Japan). Soon, these E-W aligned disturbances disappear and obvious NE-SW frontal structures form at higher latitudes in both hemispheres. This is eminent in the 10:30 UT images (b (Japan) and f (Australia)) with wavelike tilted disturbance structures. Still, the maximum amplitude of the frontal structure is significantly larger in the summer hemisphere (Japan; ∼0.47 TECU) than in the winter hemisphere (Australia; ∼0.22 TECU). Later, after around 11:30 UT, the wavebands over Japan propagate to lower latitudes (∼35°N; 50° magnetic dip) and develop rapidly over this region. The conjugate MSTIDs at lower latitudes over Australia (−50° magnetic dip) are not very clear, due to the low-amplitude perturbations and the sparse GNSS data points. At 14:00 UT, significant conjugate MSTIDs are observed within the encircled regions. From 10:00 to 14:00 UT, MSTIDs in the summer hemisphere (Japan) develop and reach the maximum intensity of 0.80 TECU, while the conjugate MSTIDs in the winter hemisphere (Australia) nearly maintain a constant amplitude (∼0.15–0.24 TECU). Ignoring the sparse distribution of GNSS data over the Australian region, the amplitude of TECPs caused by the MSTIDs in the winter hemisphere (geomagnetic conjugate region) is small.

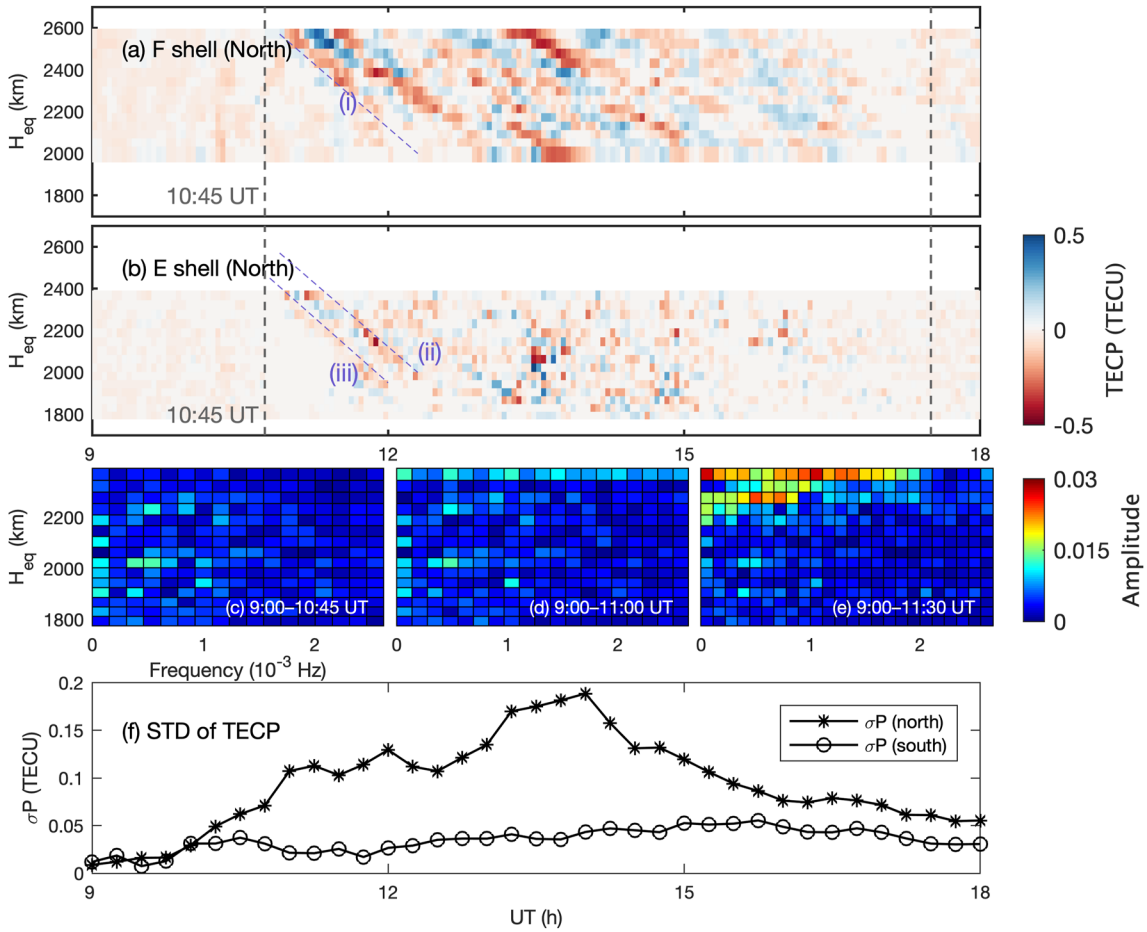

Figure 3. (a and b) Time variation of total electron content perturbations (TECPs) in E and F shells in Japan on 29 July 2019 (DOY (day of year) 210) along the northeast–southwest red dashed line in Figure 1b. H_{eq} represents the equatorial crossing height of the magnetic field line piercing each shell. Blue dashed lines indicate the alignment of evident downward-sloping stripes, and gray dashed lines represent the duration of perturbations in the F region over the analyzed area. (c–e) E-region reconstruction results of fast Fourier transform (FFT) in different time periods. (f) Time variation of the standard deviation of TECPs (σP) in different hemispheres.

Following Fu et al. (2022), the double-thin-shell approach and ground-based GNSS TEC of GEONET were used to analyze the E-F coupling process in the region with most data points over Japan (30°N–42°N, 130°E−140°E for the E shell and 28°N–45°N, 128°E−145°E for the F shell). From the results in Figures 2a–2d, this region also coincides with the fast-growing region of the MSTID structures. The parameters used in setting up and fine-tunning the algorithm are similar to those in Fu et al. (2022): two shell heights are set to 100 and 300 km for the E and F shells, respectively; in the analyzed region, the resolution in E and F shells was set to 0.15° and 0.5°, respectively; the temporal resolution is 2 min. Subplots (a–b) in Figure 3 show the time variation of TECPs on 29 July 2019 (DOY 210) during 9:00–18:00 UT (18:00–3:00 JST) along the NE-SW red dashed line in Figure 1b. H_{eq} represents the equatorial crossing height of the magnetic field line piercing each shell. The disturbances of different shells at the same H_{eq} are considered to be connected by a same magnetic field line (Fu et al., 2022). Blue dashed lines are drawn along the obvious disturbances and indicate the alignment of evident downward-sloping stripes, and gray dashed lines represent the duration of F-region perturbations over this analyzed area. Obvious disturbances in both E and F regions occur over this area after ~10:45 UT. We also performed a fast Fourier transform (FFT) analysis on the E-region reconstruction results of different time periods (from 9:00 UT to 10:45/11:00/11:30 UT) to further verify the existence of phase fronts in the E region. As shown in subplots (c–e), based on the FFT analysis, the E-region coherent sizable disturbances were detected at higher latitudes after ~10:45 UT, which confirms the phase fronts within the E-shell keograms in subplot (b). In fact, the duration of strips (i) and (ii) in subplots (a–b) is the same; the disappearance of TECP at around 12:00 UT in strip (i) is due to satellite movement, such that the IPP points drift away from the red dashed line in Figure 1b. Evident downward-sloping stripes (i) and (ii) in subplots (a–b) have similar H_{eq} and gradients, indicating the occurrence

of E-F coupling: the irregularities in different regions are connected by a magnetic field line, and share a similar NW-SE wavefront propagating to the southwest with a phase velocity of ∼100 m/s. More importantly, the small-amplitude disturbances in the E region indicated by stripe (iii) are about 30 min earlier than stripe (i) in the F region and stripe (ii) in the E region. As inferred from Figure 2, MSTIDs in Japan (summer) propagate to lower latitudes (∼35°N), and then the amplitudes develop rapidly in this region after around 11:30 UT. The earlier occurrence of Es further supports the theory that Es layer plays a major role in amplifying the Perkins instability in the F region via electromagnetic coupling along the geomagnetic field lines (Cosgrove, 2013; Yokoyama et al., 2009).

To study the MSTID activity, A. Saito et al. (2001) used the standard deviations of TECP within 1 hr to represent amplitude of TECPs caused by MSTIDs, and results show a good correlation between the standard deviation of TECP with horizontal structures of TECPs on the 2D maps. We follow the same to avoid occasional sizable errors in TECPs; for each epoch, over the whole region (either Japan or Australia), a standard deviation of TECPs (σP) is computed. Considering the propagation of MSTIDs and the less data points over Australia, this parameter can only represent the relative intensity variation over the region with most data points. In Figure 3f, the σP in different hemispheres are plotted every 15 min to indicate the time variation of the disturbance intensity, wherein the σP over Japan and Australia are represented by asterisks mark and circle, respectively. From the results in Figure 2, the ionospheric disturbances over Japan (summer) develop at higher latitudes at about 10:00 UT and reach the maximum at around 14:00 UT; disturbances show weak development in Australia (winter) during the MSTID event. Consistent with these conclusions, in Figure 3f, σP(north) (in Japan) start to increase after 10:00 UT and reach the maximum at around 14:00 UT; in Australia, the disturbance intensity (σP(south)) shows a small increase in the initial phase (at ∼10:00 UT) with the development of MSTIDs in the summer hemisphere (Japan), but then the activity of conjugate MSTIDs remains constant throughout the MSTID event.

To further validate the GNSS-TEC observation results in Japan and to supplement information on the Es layer over Australia, the ionosphere parameters provided by six ionosondes from 7:00 to 18:00 UT at DOY 210, 2019, are plotted in Figure 4 to show the variation of Es-layer intensity in conjugate regions, wherein foEs is represented by asterisks mark and fbEs by circle. Gray dashed lines represent the same as in Figure 3. Generally, the absence of values for foEs or fbEs indicates the nonexistence of sporadic or blanketing E in the ionogram at that particular time. From Figures 4a–4c, in the summer hemisphere (Japan), consistent with GNSS-TEC results in Figures 2 and 3, the variations of large foEs (>8 MHz) and foEs-fbEs (>5 MHz) values suggest that the Es layers form earlier at higher latitudes (Wakkanai), and propagate to lower latitudes (Kokubunji and Yamagawa). During this process, foEs and foEs-fbEs amplitude decreases equator-ward, indicating a gradual decrease in Es-layer activity. Similar cases can be found in Narayanan et al. (2018), where the E region structure becomes weak in the late hours of MSTID event, while the F region structure can sustain longer once formed. This is understandable because the growth time required for the MSTID formation is rather short in the E-F coupling process (Yokoyama et al., 2009). Observations at Kokubunji ionosonde, located within the region of most GNSS data points, show enhancement after 11:00 UT with maximum intensity at around 14:00 UT; this result is consistent with the E-region reconstruction results in Figure 3b. After the onset (at ∼10:45 UT) of the coupling process in the summer hemisphere (Japan), in the winter hemisphere (Australia), at Townsville and Darwin, preexisting Es layers show a reduced intensity with foEs < 3 MHz; foEs-fbEs ≈ 1 MHz; an indication of a less structured in the Es layer (Maruyama et al., 2006). Further, the Es layers over Townsville and Darwin show dissipation at around 12:00 UT and later exhibit an intermittent occurrence. As shown in Figures 2 and 3, at ∼12:00 UT, the rapid development of MSTIDs and Es layers with large foEs values over Japan (summer) suggest the occurrence of strong E-F coupling in the Northern (summer) Hemisphere; conjugate MSTIDs in the Southern (winter) Hemisphere also move over Townsville and Darwin from higher latitudes. We consider that the disruption of Es layers over Australia (winter) is most likely related to the electrodynamic factors in this particular period, since Es layer cannot easily be dissipated by simple diffusive motion once it is formed (Yokoyama et al., 2005). Additionally, after ∼17:30 UT over Townsville, the sporadic E layer reappears and shows enhancement in the late hour of the MSTID event, which may be due to the weakening of the controlling role from electrodynamic factors at this time.

We also supplement the ground-based observations with space-based observations from COSMIC occultation and Swarm satellites. Although the E-region information from COSMIC occultation have been used for statistical analysis of E-F coupling (Liu et al., 2020), here for case study, we only qualitatively analyze the E-region electron density due to the relatively low accuracy below 200 km. Same as Figure 2, the background in Figures 5a and 5b

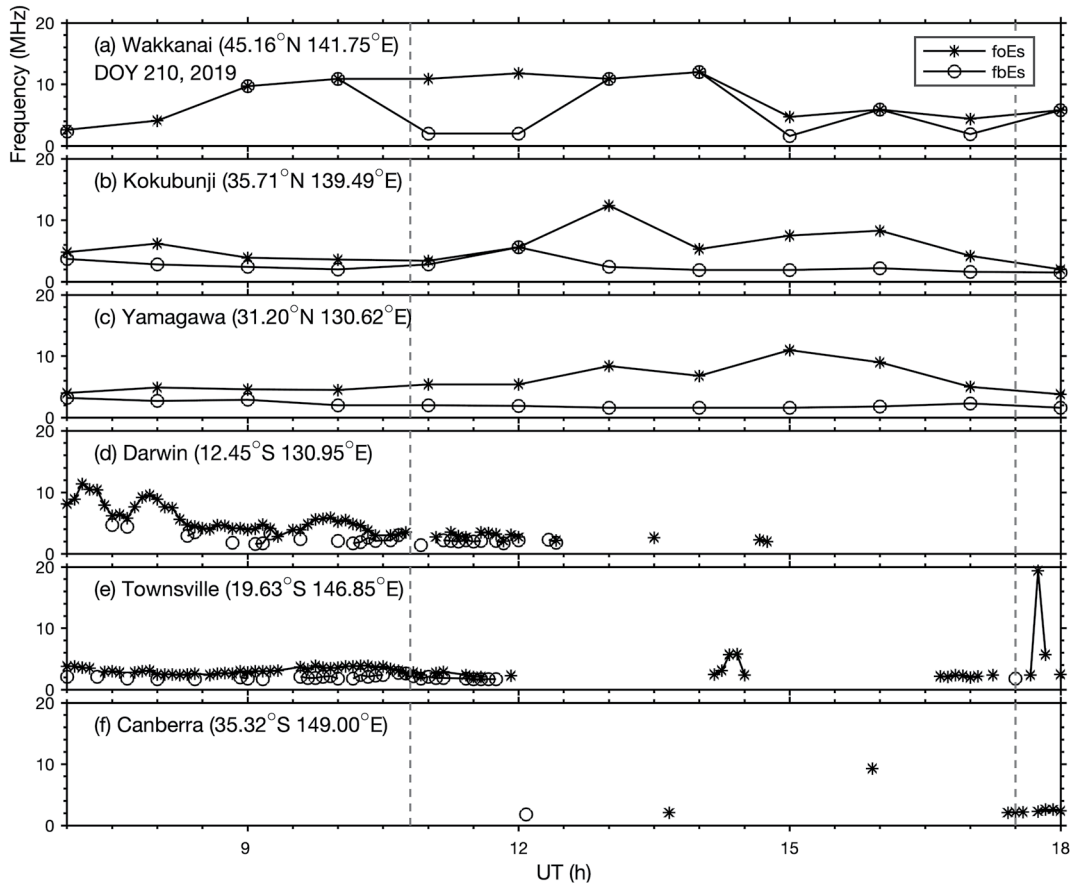

Figure 4. The ionosonde measurements from Wakkanai, Kokubunji, Yamagawa, Canberra, Townsville, and Darwin, comprising of foEs (asterisks) and fbEs (circle) from 7:00 to 18:00 UT on 29 July 2019 (DOY (day of year) 210). Gray dashed lines are the same as Figure 3, representing the duration of perturbations over the region with most data points in Japan (summer).

is the TECP maps obtained by using single-thin-shell approach at 10:45 UT, orange squares are the locations of ionosondes, and circles in different hemispheres indicate the geomagnetic conjugate regions. In Figure 5b (over the Austrian continent), the dark blue and gray solid lines are traces of COSMIC occultation tangent points; dark blue and gray represent points in ionosphere E- (below 150 km) and F-region (above 150 km) altitudes, respectively. Along each trace, gray dots show the location of the maximum electron density along the inverted density profile. The blue triangles indicate the location of the E-region peak electron densities: only included on traces when the density perturbation caused by Es is larger than the density at the E region top (~150 km). Purple lines represent the traces of Swarm satellites at around 10:45 UT, when they cross the conjugate region. Subplots (c–h) in Figure 5 show the results of COSMIC constellation vertical electron density profiles at different epochs. From the GNSS-TEC results, significant MSTIDs (maximum: 0.67 TECU) are observed at ~50°–60° magnetic dip in the summer hemisphere (in the region circled by the orange line), while the conjugate MSTIDs are weak (maximum: 0.23 TECU) in the winter hemisphere. From occultation observations over Australia (winter), no particularly strong Es layer is observed; electron density perturbations at ~100 km are relatively large in RO1 and RO2 profiles at around 8:50 and 10:30 UT; the observed Es-layer activity is low even within the conjugate MSTIDs (as inferred from RO6 trajectory and Figure 2h).

Figures 6a–6h show the observation results from Swarm satellites along the traces in Figure 5, at around 10:45 UT on 29 July 2019 (DOY 210). The two Swarm observations have a time difference of ~15 min, but this is considered minimal and the observations are analyzed as simultaneous. Following Yokoyama and Stolle (2017), magnetic field variations are obtained by subtracting CHAOS-7 model predictions for the core, lithosphere, and large-scale magnetospheric fields (Finlay et al., 2020). The first four rows in Figure 6 shows the in situ electron density, and radial (dB_L; positive outward), zonal (dB_ϕ; positive horizontal eastward), and parallel components

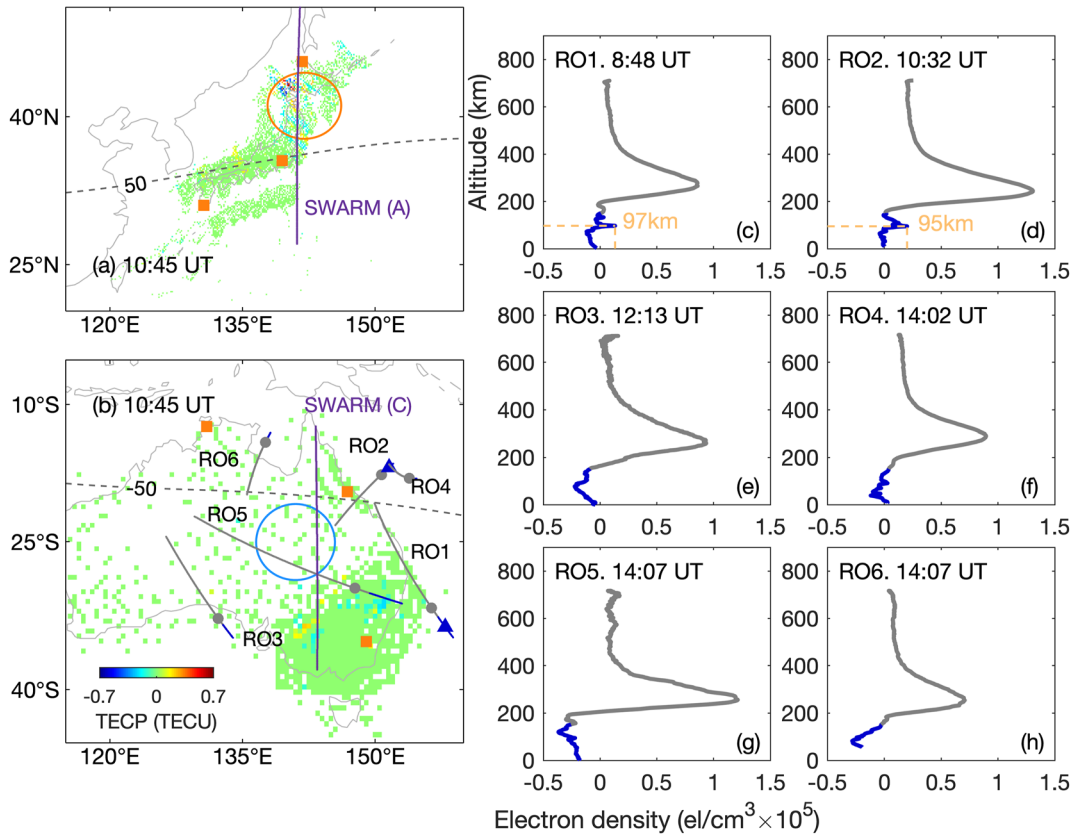

Figure 5. (a and b) Gray (dark blue) solid are traces of Constellation Observing System for Meteorology, Ionosphere, and Climate (COSMIC) occultation tangent points at F (E) region altitude and gray dots (blue triangles) are locations of maximum electron density in the F (E) region along each trace. Purple solid lines represent the traces of Swarm satellites. Background is the ground-based global navigation satellite system (GNSS) total electron content perturbation (TECP) map at 10:45 UT on 29 July 2019 (DOY (day of year) 210), orange squares are the locations of ionosondes, and circles in different hemispheres indicate the geomagnetic conjugate regions. (c–h) Results of COSMIC constellation vertical electron density profiles at different epochs.

($dB_{\parallel}$; along the mean magnetic field) of residual magnetic fields, respectively, plotted over magnetic dip. $dB_{\parallel}$ arises from diamagnetic currents owing to plasma density gradients around and within the depletions, and the magnetic field variation perpendicular to the main field direction (dB_{L} and dB_{ϕ}) is related to the field-aligned currents (Lühr et al., 2003). The field-aligned sheet current density and diamagnetic current strength are not correlated (Park et al., 2009b). Since the coupled electrodynamics between the E and F regions and between different hemispheres are accompanied by significant field-aligned currents, mid-latitude electric field fluctuations (MEFs) or mid-latitude magnetic field fluctuations (MMFs) are usually only observed in the perpendicular components with an amplitude of a few nT (Yokoyama & Stolle, 2017). Many research works have already verified the close relationship between MEFs/MMFs and nighttime mid-latitude MSTIDs (Burke et al., 2016; Park et al., 2015, 2009a; A. Saito, Iyemori, et al., 1998; Wan et al., 2020).

In Figures 6a–6h, magnitudes of MMFs in the perpendicular components (dB_{L} and dB_{ϕ}) are comparable for different hemispheres (summer hemisphere values are slightly larger), but the electron density fluctuations are much larger in the summer hemisphere (Japan), as observed by GNSS TEC in Figures 5a and 5b. Subplots (i–j) show a scatter of perpendicular components (left) and electron density with parallel magnetic field variation (right) during the nighttime MSTID event on 29 July 2019 (DOY210). The orange and blue dots correspond to the observations in summer (Japan) and winter (Australia) hemispheres, respectively. Similar to the example in Yokoyama and Stolle (2017), in subplots (c–f), perpendicular components (dB_{L} and dB_{ϕ}) depict a weak negative correlation (correlation coefficient; $r = -0.35$) in the summer hemisphere (Japan), and a near zero or no correlation ($r = 0.08$) in the winter hemisphere (Australia). The poor correlation between the perpendicular components of magnetic field variations in the winter hemisphere (Australia) could be attributed to the complicated small-scale

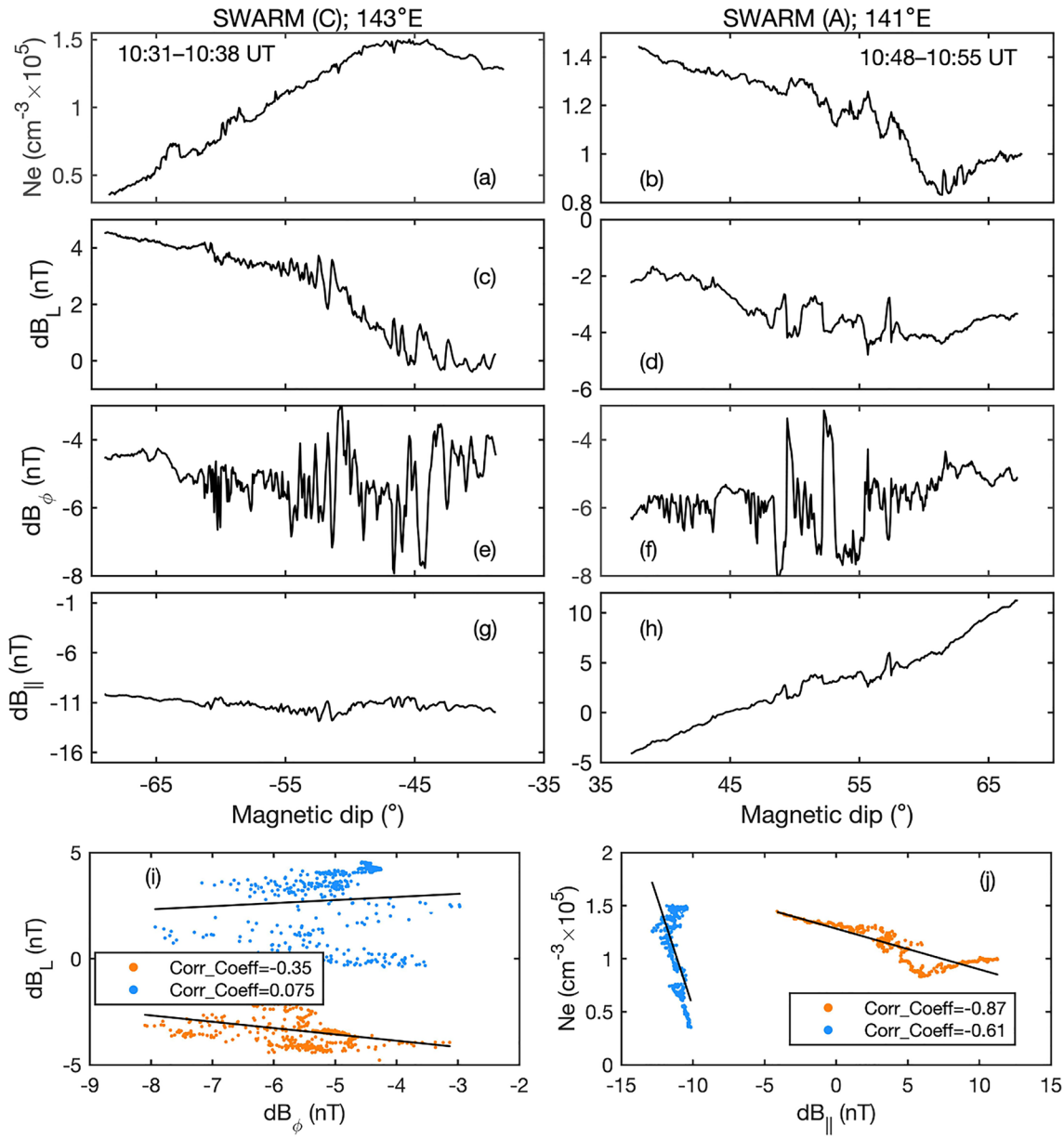

Figure 6. (a–h) In situ electron density, and radial (dB_L), zonal (dB_ϕ), and parallel components ($dB_\parallel$) of residual magnetic fields observed by the Swarm A and C satellites along the traces in Figure 5, on 29 July 2019 (DOY (day of year) 210). (i and j) A scatter of perpendicular components (left) and the electron density with parallel magnetic field variation (right) during this nighttime medium-scale traveling ionospheric disturbance (MSTID) event. The orange and blue dots correspond to the observations in summer (Japan) and winter (Australia) hemispheres, respectively.

structures (Yokoyama et al., 2015; Yokoyama & Stolle, 2017). Since Swarm A and C orbit at an altitude of ~450 km, which is above the average F2 peak density location, and MMFs and MSTIDs share similar climatology and morphology characteristics (Park et al., 2015, 2009a), then a simultaneous observation of perpendicular MMFs in conjugate regions indicates the detection of flowing inter-hemispheric field-aligned current associated with MSTIDs. As for the parallel components, the anticorrelation between density and $dB_\parallel$ is more obvious in the summer hemisphere (Japan; $r = -0.87$) than in the winter hemisphere (Australia; $r = -0.61$). This result further provides the evidence that more significant plasma density variation occurs in the summer hemisphere. This disparity could be related to the linear growth rate of the Perkins instability which is expressed as (Perkins, 1973)

$$\gamma = \frac{|\mathbf{E}^*|\cos I}{BH}\sin(\theta - \alpha)\sin\alpha \quad (1)$$

where $\mathbf{E}^* = \mathbf{E} + \mathbf{U} \times \mathbf{B}$ is the total effective electric field, $\mathbf{U} \times \mathbf{B}$ is the effective electric field, $\mathbf{U}$ is the F-region neutral wind, $\mathbf{B}$ is the geomagnetic field with a strength of B, respectively, I is the magnetic inclination angle, H is the atmospheric scale height, θ is the angle between $\mathbf{E}$ and the magnetic east direction, and α is the angle between the direction normal to the frontal structure and the magnetic east direction. According to this equation, γ is greatly affected by $\mathbf{U} \times \mathbf{B}$, since the F-region preexisting background electric field $\mathbf{E}$ due to dynamo process is much weaker compared to the $\mathbf{U} \times \mathbf{B}$ electric field component (Otsuka, 2021). Thus, under the above argument, we suggest that the poor correlations in the winter hemisphere (density and $dB_{\parallel}$, dB_{L} and dB_{ϕ}), were a result of unfavorable ionospheric background conditions for MSTID growth leading to reduced amplitudes in that hemisphere.

3.2. Event on 26 December 2019

On 26 December 2019 (DOY 360), conjugate MSTIDs in the winter hemisphere show greater intensity than the event on 29 July (DOY 210), 2019. Figure 7 shows the 2D TECP maps for this day at various epochs from 7:00 to 14:00 UT, which are obtained by using the single-thin-shell approach at 300 km height. Orange and blue circles indicate the geomagnetic conjugate regions over Australia (summer) and Japan (winter), and black solid line represents the solar terminator. Before sunset (9:00 UT; 19:00 AEST), distinct ionospheric disturbances (∼0.7 TECU) form in the region bounded by the gray solid lines over Australia (summer) at lower latitudes (∼20°S); electron density depletions with small amplitudes (∼0.2 TECU) are observed at higher latitudes (∼35°S; circled by the orange line in subplot (f)). We consider that the disturbances during the day are seeded by AGWs, because the daytime E-region conductivity is much larger than that of the F region, thus causing larger currents to close mainly in the E region and limiting polarization electric fields that could facilitate the E-F coupling (Heelis et al., 2012; Kelley, 2009). Under such conditions, the propagation direction of this disturbance structure is most likely equatorward since equatorward propagating AGWs could cause a larger amplitude of TECPs than AGWs propagating in other directions (Hooke, 1968). The density depletions at higher latitudes propagate roughly to the northwest, while the exact direction of the disturbance structure at lower latitudes is difficult to determine due to the sparse GNSS data points over this region.

At around 9:00 UT (19:00 AEST) near sunset, the AGW-seeded disturbances at lower latitudes show a drop in amplitudes and disappear (or propagate to the region beyond GNSS detection); F-region density enhancements/depletions form at higher latitudes (∼35°S; bounded by orange circle in subplot (g)). Subsequently, at ∼10:00 UT (20 AEST) after sunset, significant NE-SW aligned MSTID structures (0.32 TECU) are observed at higher latitudes (∼35°S) of Australia (summer), propagating northwestward. In the winter hemisphere (Japan), conjugate disturbances aligned in NW-SE caused by the interhemispheric coupling appear at higher latitudes (∼45°N; circled by the blue line in subplot (i)) at around 11:15 UT (20:15 JST), and then propagate to lower latitudes (∼35°N; circled by the blue line in subplot (j)) at around 12:00 UT (21:00 JST). The MSTIDs in different hemispheres are symmetric about the magnetic equator, sharing similar phase velocities of ∼100 m/s and propagating toward equator-westward direction. From 11:15–13:00 UT, the tilted disturbances over Japan (winter) develop to obvious wavelike structure. Still, the intensity of conjugate MSTIDs is larger in the summer hemisphere (0.42–0.60 TECU) than the winter hemisphere (0.15–0.34 TECU). At around 14:00 UT, the conjugate MSTIDs over Japan (winter) develop to the maximum intensity close to (but less than) that in Australia (summer).

Same as Figure 3 but for 26 December 2019 (DOY 360), Figure 8 show the time variation of E- and F-region TECPs at E- and F-shell heights, the E-region reconstruction results of FFT, and the standard deviation of TECPs (σP) in different hemispheres. For this event, in the analyzed region with most data points over Japan (winter), evident downward-sloping stripes occur after ∼12:00 UT at the F-shell height, and reach the maximum intensity at around 14:00 UT. However, at the E-shell height, noise or the mixture of noise and low-amplitude disturbances dominate, especially when the disturbance intensity is high in the F region. Similar cases were reported in the simulation section of Fu et al. (2022), where the E-region reconstruction performance deteriorates if strong disturbance exists in the F region and weak or no disturbance exists in the E region. The low development of E-region disturbances during this time period has also been verified by the FFT analysis on the E-region reconstruction in subplots (c–e), where no weak phase fronts are lurking within the noise. That is to say, in the winter hemisphere (Japan), the Es layer does not have a significant effect on the MSTIDs in the F region through local E-F coupling. This phenomenon coincides with the inference obtained from the hemisphere-coupled simulations in Yokoyama (2014); that MSTIDs in the winter hemisphere may be driven by the irregularities in the summer hemisphere through the hemisphere-coupled electrodynamics.

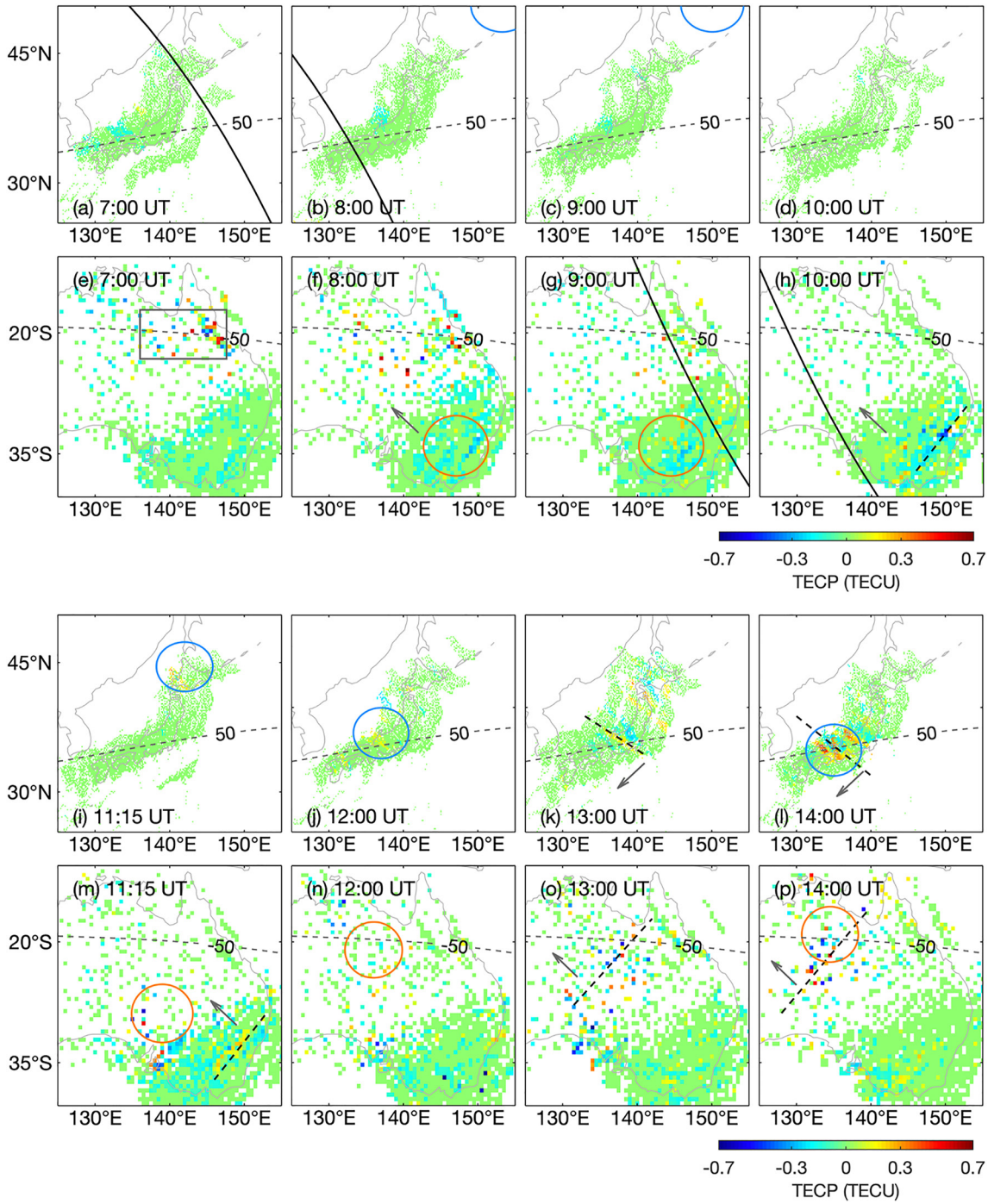

Figure 7. Same as Figure 2 but for 26 December 2019 (DOY (day of year) 360), snapshots of total electron content perturbation (TECP) maps at various time epochs from 6:00 to 14:00 UT. Gray dashed lines represent the magnetic dip at ±50°, solid orange and blue circles indicate the geomagnetic conjugate regions over Australia (summer) and Japan (winter), black solid line represents the solar terminator, rectangle bounded by gray solid line indicates the region where disturbances occur before sunset, black dashed lines indicate the alignment azimuths of the apparent frontal structures, and gray arrows denote the drift direction.

The standard deviations of TECPs (σP) in different hemispheres on 26 December 2019 (DOY 360) are plotted in subplot (f) to indicate the time variation of disturbance intensity. Results indicate that disturbances are continuously observed over Australia (summer) but with a reduction in amplitude after ~14:00 UT; over Japan (winter), MSTID structures form after ~11:15 UT, and develop to the maximum intensity at around 14:00 UT; the conjugate MSTIDs in the Japan (winter) decay more rapidly compared to MSTIDs in Australia (summer). It

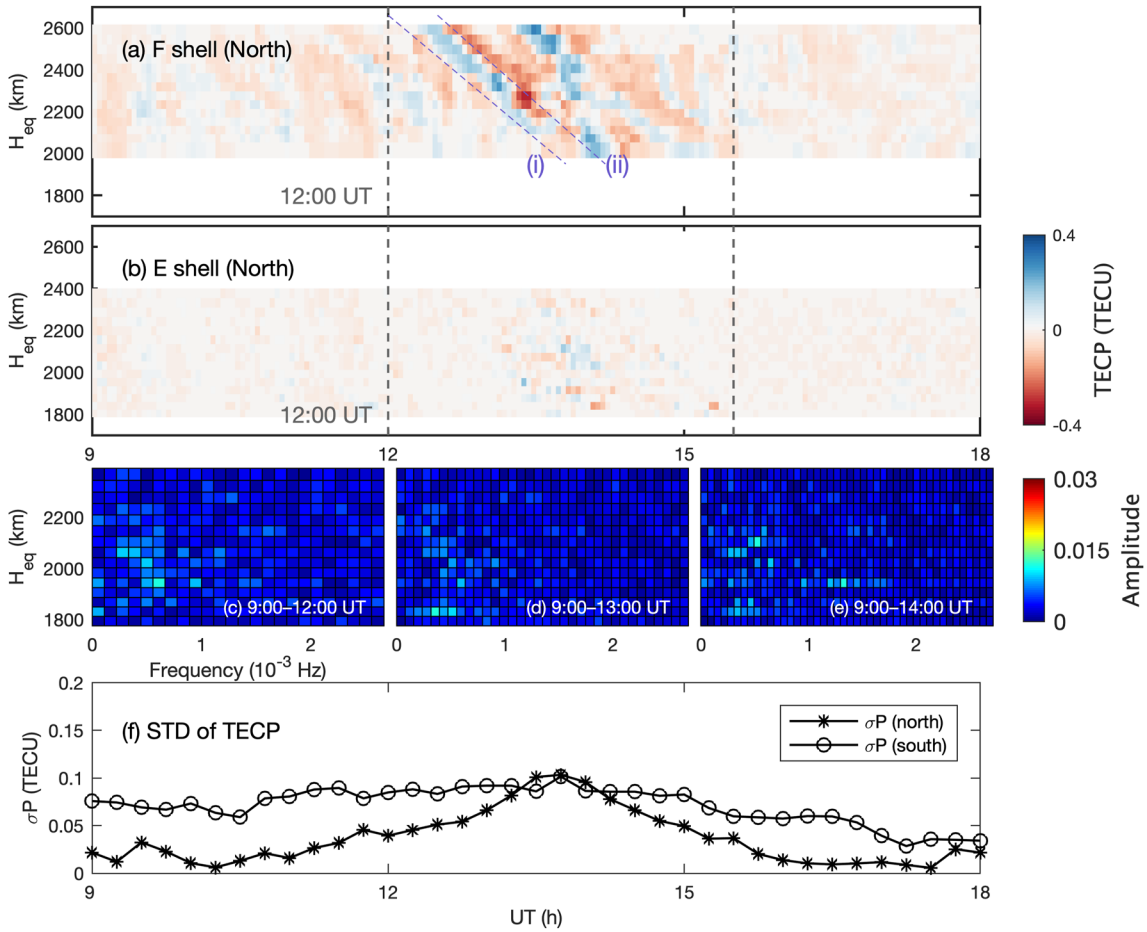

Figure 8. Same as Figure 3 but for 26 December 2019 (DOY (day of year) 360). (a and b) Time variation of total electron content perturbations (TECPs) in E and F shells along the northeast–southwest red dashed line over Japan in Figure 1(b). (c–e) E-region reconstruction results of FFT in different time periods. (f) Time variation of the standard deviation of TECPs (σP) in different hemispheres.

is important to note that at around 14:00 UT when σP reaches its maximum in both hemispheres, but the MSTID intensity is still larger in Australia (summer) but the sparse data points limit the exact representation of the intensity. Compared to the variation of σP in Figure 3, the maximum amplitude of disturbance (σP) over Japan is reduced by half, while that over Australia region is doubled.

To obtain more information on E-region activity in both hemispheres, we have plotted ionosphere parameters provided by ionosondes in Figure 9 as in Figure 4, but for event 26 December 2019 (DOY 360). The labels mean the same as in Figure 4. The time is from 5:00 to 18:00 UT. Gray dashed lines represent the duration of the perturbations over the region with most data points in Japan (winter), as in Figure 8. Similar to the Es-layer variation in the winter hemisphere discussed in the previous section, frequently observed Es layers with small amplitudes (foEs < 5 MHz, foEs-fbEs < 2.5 MHz) over Wakkanai, Kokubunji, and Yamagawa show reduced foEs (<3 MHz) and foEs-fbEs (<1 MHz) values during the interhemispheric coupling process. The ionograms over Wakkanai, Kokubunji, and Yamagawa during 12:00–15:30 UT further validate the results obtained by using the double-thin-shell approach in Figures 8a and 8b, that is, the Es layer has a very low development during the conjugate MSTIDs in the winter hemisphere (Japan). In the Southern Hemisphere (summer), as observed by the ground-based GNSS TEC in Figure 7, ionospheric F-region disturbances occur over Australia before sunset. Before 9:00 UT (19:00 AEST), sporadic and blanketing E layers over Townsville and Darwin at lower latitudes are frequently observed in the ionograms, which may be associated with the daytime sporadic E activity or the irregularities observed before sunset. At 9:00 UT, both foEs and the difference between foEs and fbEs show enhancement over the Canberra ionosonde, followed by the formation of distinct NE-SW aligned frontal structures in this region as shown in Figures 7g and 7h, from which the occurrence of E-F coupling in the Southern

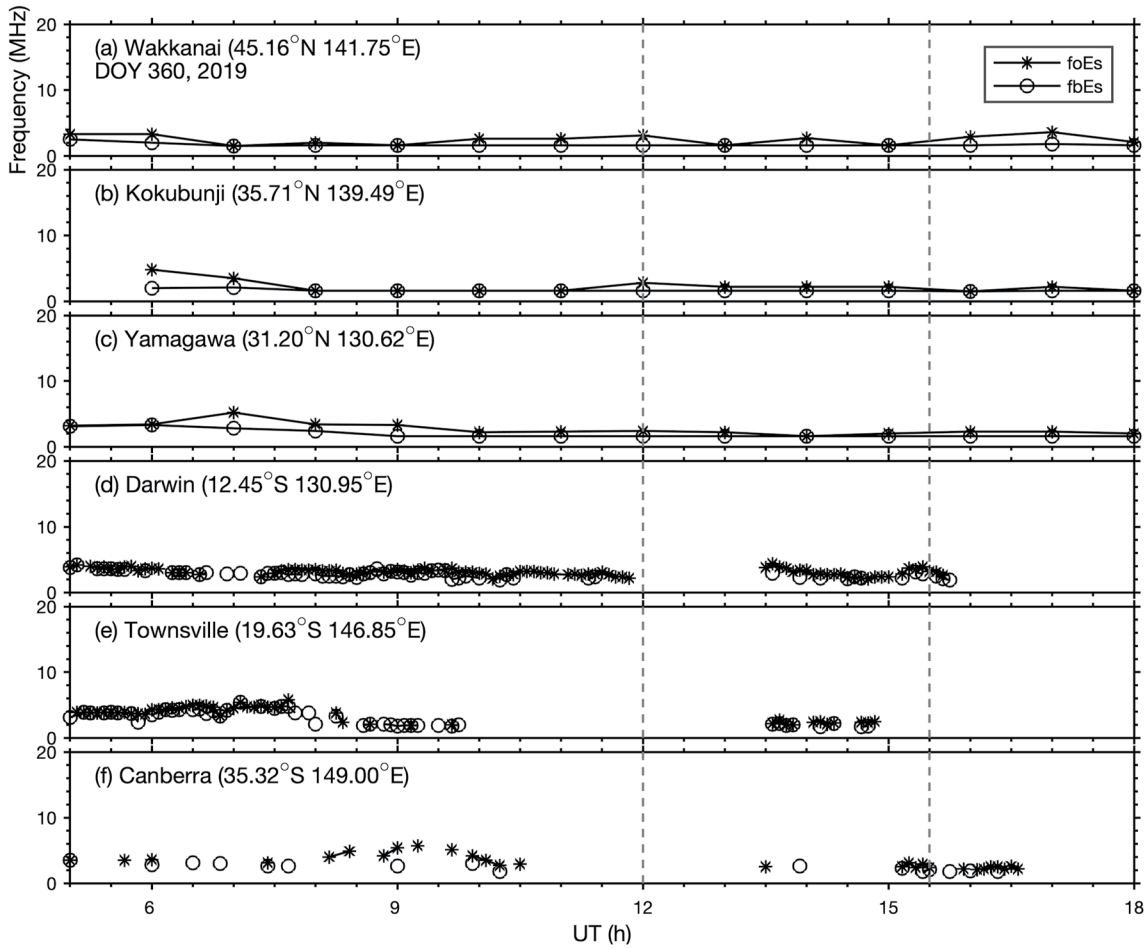

Figure 9. The ionosonde measurements from Wakkanai, Kokubunji, Yamagawa, Canberra, Townsville, and Darwin, comprising of foEs and fbEs from 5:00 to 18:00 UT on 26 December 2019 (DOY (day of year) 360). Gray dashed lines are the same as Figure 8, representing the duration of perturbations over the region with most data points in Japan.

Hemisphere can be inferred. Subsequently, in Figures 9e and 9f, after the onset of local E-F coupling, the Es layers coupled with MSTIDs are observed at lower latitudes, at 13:30 UT, over Townsville and Darwin. It is worth noting that, at around 9:00 UT, the foEs (<6 MHz) and foEs-fbEs (<3 MHz) in the summer hemisphere (Australia) on DOY 360 in Figure 9 are significantly less than those on DOY 210 in Figure 4. One reasonable explanation is that the Es plasma density is higher in Japan (Northern Hemisphere) around the June solstice than in Australia (Southern Hemisphere) around the December solstice (Wu et al., 2005), and the E-region conductivity near the solar terminator is still large enough to short out the polarized electric field. Or, the presence of MSTIDs seeded by AGWs may have generated favorable conditions to the development of the Perkins instability, for example, enhanced background electric field (Yokoyama, 2014), which makes the effects of Es layer in the E-F coupling become less pronounced.

Same as Figure 5 but for 26 December 2019 (DOY 360), Figure 10a shows the 2D TECP map at 9:15 UT (19:15 AEST) and traces of space-based observations including Swarm (purple lines), COSMIC (gray and dark blue lines), and ICON-MIGHTI (blue line). At around 9:15 UT, the NE-SW aligned frontal structures start to form and develop at higher latitudes in the summer hemisphere (Australia; in the vicinity of the orange circle region), while no disturbances are observed by GNSS-TEC in the winter hemisphere (Japan). Subplots (c–d) show the meridional and zonal wind profiles (positive northward and eastward) measured by ICON-MIGHTI at the locations shown by the blue solid line in subplot (b). As observed in Figure 7, at 9:15 UT the solar terminator is crossing Australia. Due to the high activity of AGWs in the solar terminator (Forbes et al., 2008), the ICON-MIGHTI data along this trajectory have many blanks: Otsuka (2021) briefly discusses that the vertical wavelength of AGWs

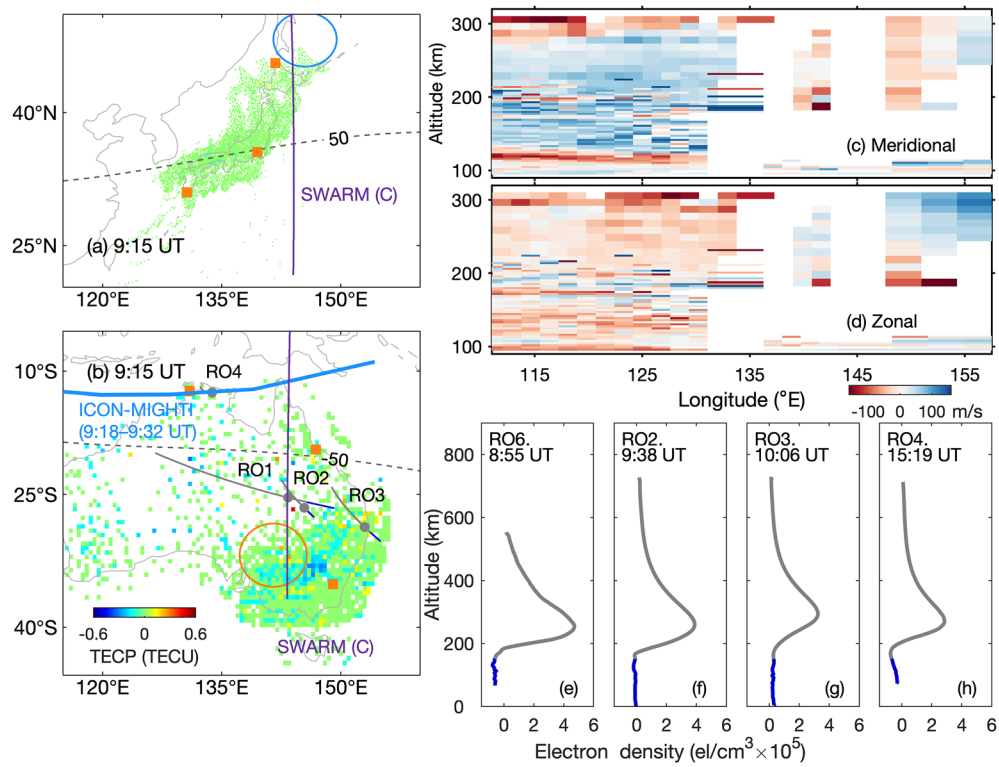

Figure 10. (a and b) Gray (dark blue) solid lines are traces of Constellation Observing System for Meteorology, Ionosphere, and Climate (COSMIC) occultation tangent points in F (E) region, gray dots are locations of maximum electron density along each trace, and orange and blue circles indicate the conjugate regions in the summer and winter hemispheres. Purple and blue solid lines represent the traces of Swarm satellites and Ionospheric Connection Explorer (ICON)-Michelson Interferometer for Global High-resolution Thermospheric Imaging (MIGHTI) neutral winds, respectively. Background is the ground-based global navigation satellite system (GNSS) total electron content perturbation (TECP) map at 9:15 UT on 26 December 2019 (DOY (day of year) 360). (c and d) Meridional and zonal wind profiles (positive northward and eastward) measured by ICON-MIGHTI at the same locations above. (e–h) Results of COSMIC constellation vertical electron density profiles at different epochs.

is affected by the background neutral wind, with waves propagating against the background winds exhibiting longer intrinsic vertical wavelength and reaching higher altitudes. In due process, to conserve kinetic energy, the amplitude of the neutral wind oscillation increases (which in return affects the airglow profiles). Therefore, we think, it is this rapid variation in the profiles that leads to increased error in the retrieved wind data, thus rendering the data unusable. The data continuity is good on the dusk side (110°E−135°E), and the results indicate that at ∼200-km altitude, the equatorward and westward neutral winds prevail over this area before sunset. On the night side (135°E−160°E), the thermospheric winds show great fluctuations. However, we found that on the night side, the neutral wind conditions in the E region can support the generation of the Es layer, since wind shear is observed in both meridional and zonal directions over this area (Haldoupis, 2012). In fact, this wind shear indeed amplified the Es layer: as shown in Figure 9, over Darwin in the vicinity of the observation area, (foEs-fbEs) show enhancement (from <1 to 1.7 MHz) at around 9:40 UT after sunset. In addition, no significant electron density perturbations caused by Es layer are observed by COSMIC occultation for this MSTID event. Since GNSS-TEC observations are sensitive only to ionospheric disturbances with high electron density (or large foEs) (Maeda & Heki, 2014), occultation events at ∼9:00–10:00 and 15:00 UT do not capture the weak Es layers (∼4 MHz) observed by Townsville and Darwin ionosondes, even in RO4 event close to Darwin.

Figures 11a–11h show the observation results of in situ electron density, dB_L, dB_ϕ, and $dB_\parallel$, from Swarm satellites along the traces in Figures 10a and 10b, at around 9:00 UT on 26 December 2019 (DOY 360). The derivation method of the residual magnetic field is the same as that used for Figure 6. At higher latitudes in the Northern Hemisphere (winter) beyond GNSS detection (>55° magnetic dip; within the blue circle region in Figure 10a), drops and perturbations in electron density are observed without accompanied MMFs. We think this structure

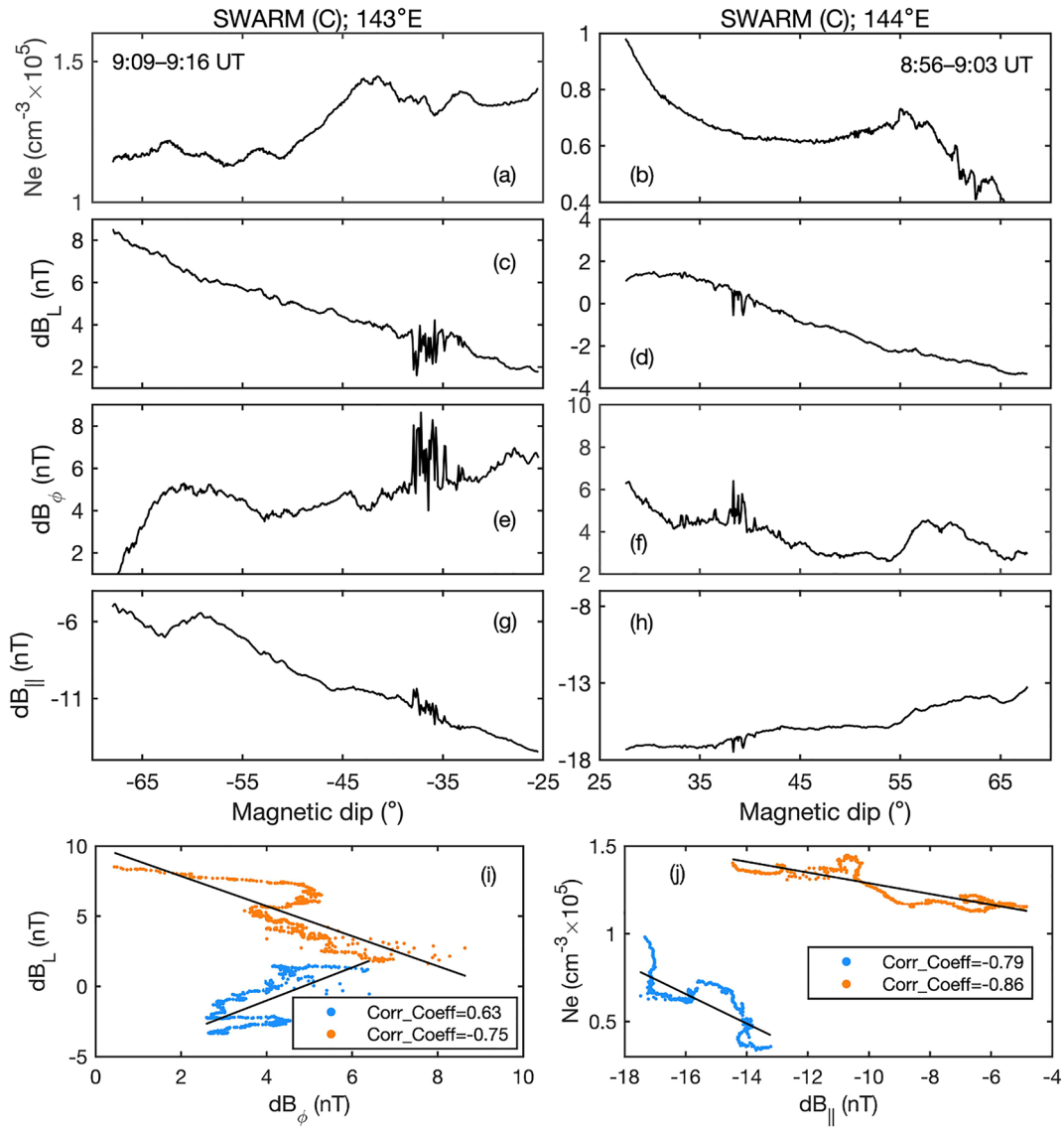

Figure 11. (a and b) In situ electron density, and radial (dB_L), zonal (dB_ϕ), and parallel components ($dB_\parallel$) of residual magnetic fields observed by the Swarm A and C satellites along the traces in Figure 10, on 26 December 2019 (DOY (day of year) 360). (i–j) A scatter of perpendicular components (left) and the electron density with parallel magnetic field variation (right) during this nighttime medium-scale traveling ionospheric disturbance (MSTID) event. The orange and blue dots correspond to the observations in summer (Australia) and winter (Japan) hemispheres, respectively.

may be the results of nighttime midlatitude ionospheric trough, which is mainly driven by neutral winds (He et al., 2011). In the Southern Hemisphere (summer), relatively moderate electron density variations are detected at −40° to −30° magnetic dip, which could be the same disturbances seeded by AGWs we observed before sunset as shown in Figure 7e. The speculation of AGWs is supported by the thermospheric wind observations in Figures 10c and 10d, wherein significant variations exist in the lower F region (~200 km in both meridional and zonal directions). Near this region, the AGWs would presumably be the strongest since AGWs propagating against the background winds can propagate vertically to higher altitudes and then weaken due to viscosity and thermal conductance (Pitteway & Hines, 1963). Due to the limited distribution of GNSS distribution, this disturbance structure is not observed by GNSS TEC in Figure 10a. The fluctuations caused by this disturbance are observed in both perpendicular (dB_L, dB_ϕ) and parallel ($dB_\parallel$) components of residual magnetic fields in the conjugate regions (~±37° magnetic dip) of both hemispheres, as shown in Figures 11c–11h. However, different from the results in Figure 6, the intensity and magnitude of these magnetic field fluctuations in the summer hemisphere

(Australia) are significantly greater, which could be caused by the differences in ionospheric conductivity and electric field between these two geomagnetic conjugate regions (Park et al., 2009a). That is, MMFs amplitudes are related to field-aligned currents which are dependent on the effective electric field ($\mathbf{E}^* = \mathbf{E} + \mathbf{U} \times \mathbf{B}$) and ionospheric conductivity, that are larger in the summer hemisphere since the F-region conductance is proportional to the plasma density (Lee et al., 2021) and equatorward wind ($\mathbf{U}$) which is larger in the summer hemisphere (Tepley et al., 2011).

In the GNSS-TEC observations of Figure 10b, at −65° to −60° magnetic dip (within the orange circle region) in the Southern Hemisphere (summer) before sunset, MSTIDs form with a small amplitude. In the subplot (a) of Figure 11 at around 9:15 UT, small-scale undulations of in situ electron density are also observed by Swarm A satellite in the corresponding region. However, compared to the developed MSTID structures at lower latitudes (−35° magnetic dip), fluctuations with large wavelengths but small intensities are observed only in dB_ϕ and $dB_\parallel$ in geomagnetic conjugate regions. The fact that no corresponding perturbations in dB_L indicates that the field-aligned currents are small in the initial phase of MSTID development, and the perturbations in dB_ϕ could be related to the apparent zonal propagation of AGWs caused by solar terminator (Forbes et al., 2008; Miyoshi et al., 2009; Somsikov, 2011). Subplots (i–j) in Figure 11 show a scatter of the variation in magnetic field perpendicular components (left), and electron density with parallel magnetic field variation (right), during the nighttime MSTID event on 26 December 2019 (DOY 360). The orange and blue dots correspond to the observations in summer (Australia) and winter (Japan) hemispheres, respectively. Negative correlations between electron density and parallel magnetic field variation are observed in both hemispheres ($r = -0.86$ and -0.79 for the summer (Australia) and winter (Japan) hemispheres, respectively); dB_L and dB_ϕ show anticorrelation in the summer hemisphere (Australia; $r = -0.75$) and correlation in the winter hemisphere (Japan; $r = 0.63$). Although these correlations/anticorrelations are still weaker in the winter hemisphere compared to the summer hemisphere, the performance is improved compared to the results in Figure 6, especially in the perpendicular components (dB_L and dB_ϕ). We suggest that such ionospheric background conditions (e.g., effective electric field $\mathbf{U} \times \mathbf{B}$) favor the Perkins instability growth (as described in Equation 1) and persist for some time (until the maximum amplitude of MSTIDs at around 14:00 UT), which subsequently lead to the formation of geomagnetic conjugate MSTID structures in the winter hemisphere, with maximum amplitudes close to those in the summer hemisphere.

4. Discussion

4.1. Controlling Role of Es in the Summer Hemisphere

This study used two nocturnal mid-latitude MSTID events in July and December 2019 to analyze the E-F coupling in the geomagnetic conjugate regions. Although 2019 is the year of low solar activity, this does not affect our analysis on the mechanisms of local and interhemispheric coupling (Otsuka et al., 2021). For both events, from GNSS-TEC observations in Figures 2 and 7, MSTID structures with preferred direction were observed in the summer hemisphere. However, in the winter hemisphere, conjugate MSTIDs with different amplitudes were formed on 29 July 2019 (DOY 210) and 26 December 2019 (DOY 360). Yokoyama (2014) suggested that MSTIDs observed in the winter hemisphere may be driven by the Es layer in the summer hemisphere. Narayanan et al. (2018) have found that the presence of Es layers in one hemisphere is sufficient enough to form conjugate MSTIDs. Lee et al. (2021) concluded that conjugate MSTIDs in the winter hemisphere are associated with MSTIDs in the summer hemisphere; the summer hemisphere MSTIDs are related with the occurrence of Es in the summer hemisphere. To further verify and specify this conclusion on a larger scale, we simultaneously analyzed the E- and F-region horizontal structuring and evolution over Japan by using GNSS TEC and a double-thin-shell approach, when electrodynamic influenced irregularities (Es and/or MSTIDs) are present. In Figures 3 and 8, over the analyzed region during MSTID event, Es layers were observed only in the summer hemisphere and appear ∼30 min earlier than the MSTIDs in the F region; in the summer hemisphere, the coupled E- and F-region disturbances share similar alignment, propagation direction, and phase velocity, and are related to each other through a magnetic field line; conjugate MSTIDs in the winter hemisphere appear later and disappear earlier than the MSTIDs in the summer hemisphere. These results further support the evidence that the F-region conjugate structures in both hemispheres are mainly driven by the Es layer in the summer hemisphere through local E-F coupling and interhemispheric coupling. Furthermore, it might be also reasonable to assume that the phase velocity of geomagnetic conjugate structures are controlled by the E-region neutral wind velocities in the summer hemisphere due to the comparable velocities and the important role of E-region meridional wind in MSTID

propagation (Larsen, 2002; Yokoyama et al., 2009). Earlier simulation works of Tsunoda (2006) and Yokoyama et al. (2009) emphasized the contribution of the neutral winds in the Es layer on the MSTID propagation: even without the background electric field, the rotational wind shear in the E region produces southwest phase propagation in both E and F regions for the NW-SE structures; however, these structures are stationary if the E-region meridional wind is absent.

4.2. Decrease in Es-Layer Intensity in the Winter Hemisphere

From ionosonde observations in Figures 4 and 9, continuous Es layers with small amplitudes (foEs < 3 MHz) in the winter hemisphere show further intensity reduction and dissipation after the interhemispheric coupling. In fact, in earlier works, for example, Narayanan et al. (2018), the amplitude reduction and dissipation of Es may have been observed. However, the limited observation area in comparison to the scale of MSTIDs limited their conclusions on the temporal relationship between the occurrence of Es and MSTIDs. Further investigations have shown that under quiet conditions, the vertical structure of electric field arising from sunset electrodynamic processes can result in the enhancement or disruption of Es layer (Abdu et al., 2014): at nighttime, when E-region conductivity is significantly reduced, and the closure path for the wind-driven currents in the F region is limited, the ions drift with the neutral gas to reduce the collisional force. Thus, the distribution of winds and conductivity will subsequently modify the distribution of ionization and thereby change the ionospheric conductivity and the ion drag on the neutral gas (Heelis et al., 2012). In the E-region polarization process (Es-layer instability), when the electron density in Es has an elongated structure from NW to SE, large polarization electric fields can be generated in the direction of NE and SW (Cosgrove & Tsunoda, 2002). Now, if the integrated Pedersen conductivity in the region above Es is comparable to that within the Es patch, the polarization electric field will be reduced accordingly (Haldoupis et al., 2003). In addition, the variation of the integrated Pedersen conductivity in the F region is large during the MSTID formation (Yokoyama et al., 2009). Therefore, the preexisting Es layer is easier to show intensity reduction or even dissipation in the winter hemisphere, with a reasonable inference that the polarization electric field within the small-amplitude Es layers (foEs < 3 MHz, foEs-fbEs < 1 MHz) is small, and the integrated Pedersen conductivity within Es is easily comparable to that above Es when interhemispheric coupling occurs.

For the MSTID event on 29 July 2019 (DOY 210), only small-amplitude conjugate structures formed in the F region of the winter hemisphere (Australia). Es layers in the winter hemisphere (Australia) start to show intensity reduction and dissipation when conjugate MSTIDs move over the region. During this period, poleward meridional wind could be dominant in the Southern Hemisphere (winter), as it can push the plasma to lower altitudes where enhanced recombination occurs, thus reducing the amplitude of conjugate structures and enhancing the Pedersen conductance (Shiokawa, Otsuka, et al., 2003). For another event on 26 December 2019 (DOY 360), conjugate MSTIDs in Japan (winter) develop to a maximum amplitude close to that in Australia (summer). In such cases, equatorward thermospheric winds in both hemispheres can be inferred during the formation of conjugate MSTIDs, which favor the MSTID generation (Yokoyama, 2014). However, in the solstice period, meridional thermospheric winds at midlatitudes are not perfectly symmetric and often have a trans-equatorial component from summer to winter hemisphere (Tepley et al., 2011). Of course, the smaller equatorward wind in the winter hemisphere results in a larger Pedersen conductance in that hemisphere, but certainly not with the same effect as the poleward wind. For this event, Es layers in the winter hemisphere (Japan) start to decrease in amplitude (~12:00 UT) about 1 hr after the appearance of conjugate disturbances over Japan (~11:15 UT), that is, when conjugate MSTIDs develop to a certain magnitude. Based on the above results, we suggest that the variation in integrated Pedersen conductivity leading to amplitude reduction or even dissipation of the low-amplitude Es layer in the winter hemisphere is influenced by conjugate MSTIDs and thermospheric winds (in that hemisphere), but the former is more pivotal. Due to the nature of our results and sensitivity of data used in analysis, we could not ascertain the impact of a dissipating weak Es-layer (in winter hemisphere) on the summer hemisphere dynamics. However, based on previous simulation results, for example, Yokoyama (2014), this impact would be limited on the Es in the winter hemisphere.

4.3. Thermospheric Wind

Thermospheric winds could play an important role in the MSTID generation and development, since the effective electric field ($\mathbf{U} \times \mathbf{B}$) dominates the linear growth rate of Perkins instability, as we described in Equation 1. These

winds are not significantly affected by the MSTID formation because the time constant of the ion drag affecting the neutral wind is usually larger than the period of MSTIDs (Narayanan et al., 2018). At night when the E region conductivity is small, the thermospheric wind dynamo fluctuations can produce polarization electric fields in the F region; partially shorted out by the conductivity in the local E region or conjugate hemisphere (Buonsanto & Foster, 1993; Chen et al., 2020). Usually this phenomenon is accompanied by equatorward meridional winds (Buonsanto et al., 1990), which has been validated by the thermospheric wind measurements made with the Fabry-Perot interferometer (FPI) (Narayanan et al., 2018). Yokoyama (2014) have found through simulations that NW-SE (NE-SW) oriented MSTIDs occur simultaneously in geomagnetic conjugate regions of the Northern (Southern) Hemisphere, if F-region neutral wind satisfies the unstable condition (equator-eastward) in both hemispheres and a sporadic-E layer is given only in the summer hemisphere.

From the subplot (f) in Figures 3 and 8, the similarity of σP variation curves and the difference in amplitude between July and December in Japan may imply that local thermospheric winds play an important role in determining the level of MSTID activity. On 26 December 2019 (DOY 360), in Australia (summer), NE-SW aligned MSTIDs form at around 9:00–10:00 UT. From FPI observations over Darwin (https://stdb2.isee.nagoya-u.ac.jp/omti/data/html/fp04/2019/FP042191226_wind.html), equator-eastward meridional winds were observed (maximum at ∼12:00 UT) and turned zero or weak poleward at about 14:00 UT. After the rapid reduction or redirection of meridional wind at 14:00 UT, MSTIDs in the summer hemisphere show a decrease in both amplitude and scale. In the Northern Hemisphere (winter), NW-SE aligned conjugate MSTIDs propagate to Japan at around 11:15 UT; after 2–3 hr of development, conjugate MSTIDs develop to an intensity close to that of the summer hemisphere; subsequently, the intensity of conjugate MSTIDs decreases rapidly. We infer that the thermospheric winds in the Northern Hemisphere (winter) are most likely equator-eastward during 11:15–14:00 UT; after 14:00 UT, the thermospheric winds in both hemispheres show a decrease in amplitude and a shift in direction; the intensity of conjugate MSTIDs in Japan (winter) decreases with a much larger rate than that in Australia (summer), which could be related to the decoupling of the winter hemisphere from the summer hemisphere. As for the other event on 29 July 2019 (DOY 210), as we previously inferred, poleward meridional winds prevail in the winter hemisphere, which is unfavorable for Perkins instability. Under such condition, only conjugate MSTIDs with a small amplitude were observed in the winter hemisphere. The generation of this conjugate structure could be associated with the effective $\mathbf{U} \times \mathbf{B}$ background electric field in the hemisphere coupled ionosphere (Narayanan et al., 2018). Moreover, from Figures 6 and 11, we can also infer that ionospheric background conditions in the winter hemisphere can in turn affect the field-aligned current sheets associated with NW-SE or NE-SW aligned MSTID structures in the summer hemisphere. The correlation coefficient (r) for perpendicular components (dB_L, dB_ϕ) in the summer hemisphere is −0.35 on 29 July 2019 (DOY 210) when ionospheric background conditions in the winter hemisphere are not favorable for Perkins instability ($r = 0.08$). However, it improved to −0.75 on 26 December 2019 (DOY 360) when ionospheric background conditions in the winter hemisphere satisfy the conditions for Perkins instability ($r = 0.63$). Similar cases were also observed by simulation in Yokoyama (2014) that even if the instability conditions are satisfied in the summer hemisphere, unfavorable F-region thermospheric winds in the winter hemisphere will largely suppress the growth of MSTIDs in both hemispheres.

4.4. Amplitude Asymmetry of Conjugate MSTIDs

For both events, the MSTIDs were observed more intense in the summer hemisphere. Several factors could be associated with the amplitude asymmetry of conjugate MSTIDs in different hemispheres, for example, thermospheric wind, non-equipotential magnetic field line, and background TEC. Narayanan et al. (2018) found that the amplitude of conjugate MSTIDs tend to differ in different hemispheres particularly in the later hours after their formation. Our GNSS observations on 29 July 2019 (DOY 210) further validated this conclusion, because the conjugate MSTIDs in the winter hemisphere maintain a weak development, while the amplitude difference reaches its maximum when the MSTIDs in the summer hemisphere develop to the maximum intensity after a few hours. In addition, for the event on 26 December 2019 (DOY 360) when thermospheric winds satisfy the Perkins instability in both hemispheres, this amplitude difference is more pronounced in both early and late stages of MSTID development in the winter hemisphere, often greater than 50%.

As we inferred previously in Section 4.3, in the winter hemisphere, the meridional components of thermospheric winds are poleward on 29 July 2019 (DOY 210) and weak equatorward (compared to the summer hemisphere) on 26 December 2019 (DOY 360), respectively. Compared to the condition in the summer hemisphere, the meridional

winds in the winter hemisphere will push plasma to the lower altitudes where recombination enhances, thus reducing the ambient plasma densities and the amplitude of conjugate MSTIDs (in return increasing the Pedersen conductivity). Moreover, magnetic field lines are not perfectly equipotential after MSTID formation due to the current closure in the ionosphere through field-aligned current (Yokoyama, 2014). As we discussed in Section 4.1, the Es layer in the summer hemisphere drives the conjugate MSTIDs in both hemispheres. That is to say, the mapping efficiency of polarization electric field should be higher from the E region in the summer hemisphere to the F region in the summer hemisphere than to the F region in the winter hemisphere (Yokoyama, 2014). In such cases, the finite mapping efficiency of an electric field from the summer hemisphere to the winter hemisphere should be considered, which is positively related to the spatial scales of irregularities and negatively related to the integrated Pedersen conductivity (Farley Jr, 1959; Yokoyama et al., 2004). Therefore, the combination effect of mapping efficiency and thermospheric wind may reduce the polarization electric field in the winter hemisphere, leading to a weakening of the amplitude of conjugate MSTIDs in the winter Hemisphere.

Further, the slower growth rate of conjugate MSTIDs in the winter hemisphere may also be caused by the weaker polarization electric field mapping from the summer hemisphere. From Figures 7 and 9, E-F coupling process in Australia (summer) started at ∼9:00 UT and distinct NE-SW aligned structures were observed at ∼10:00 UT (0.32 TECU). In the opposite hemisphere, conjugate disturbances were first observed over Japan at ∼11:15 UT and formed wavelike structures over this area at ∼13:00 UT (0.30 TECU). That is, in the winter hemisphere, the smaller F-region conductivity and effective electric field $\mathbf{U} \times \mathbf{B}$ may lead to a smaller growth rate of the coupled instability (Es-layer instability coupled to Perkins instability (Tsunoda, 2006)). Thus, the time required for the growth of conjugate MSTIDs in the winter hemisphere through interhemispheric coupling is longer (about 1 hr) than that in the summer hemisphere that is amplified through local E-F coupling.

In addition, the asymmetry of background TEC could also be an explanation for the asymmetry of conjugate MSTIDs in different hemispheres. The field-line-integrated electric current in the F region, $\mathbf{J}_P$, can be expressed as (Otsuka et al., 2007)

$$\mathbf{J}_P = \Sigma_P \mathbf{E}^* \tag{2}$$

where $\mathbf{E}^* = \mathbf{E} + \mathbf{U} \times \mathbf{B}$ as in Equation 1, and Σ_p is the field-line-integrated Pedersen conductivity. Due to the existence of the electrified MSTIDs, the perturbation of electric fields (δE) and Pedersen conductivity ($\delta\Sigma_P$) should satisfy $\mathbf{J}_P = (\Sigma_P + \delta\Sigma_P)(\mathbf{E}^* + \delta\mathbf{E}^*)$. Ignoring higher-order terms and asserting current continuity, then we can have

$$\delta E \approx -\frac{\delta\Sigma_P}{\Sigma_P}\mathbf{E}^*. \tag{3}$$

Because the $\frac{\delta\Sigma_P}{\Sigma_P}$ suitably represents MSTID intensity, the latter is also proportional to δE: in this paper, we analyze integrated densities that also suitably represent MSTID intensity. Therefore, the TECP to background TEC ratio can be considered analogous to $\frac{\delta\Sigma_P}{\Sigma_P}$ and proportional to δE; with this argument, if the electric field is transmitted between different hemispheres along the magnetic field lines without attenuation, then in a given hemisphere, TECP changes should follow those of background TEC to maintain the δE (in Equation 3) constant; this could also be the reason why TECP is larger (smaller) in the summer (winter) hemisphere, where background TEC is larger (smaller).

5. Conclusions

In this paper, we used the ground-based GNSS observations to study the E-F coupling in geomagnetic conjugate regions over Japan and Australia, supplemented by data from ionosondes, COSMIC radio occultation, Swarm satellite constellation, and ICON spacecraft. Two different event days of nighttime midlatitude MSTIDs on 29 July 2019 (DOY 210) and 26 December 2019 (DOY 360), were analyzed in detail. The research presented here provides observations and analysis for the causes and effects of the E-F coupling in the interhemispheric coupled ionosphere, thus deepening our understanding of the generation mechanism of nighttime midlatitude MSTIDs. The results and conclusions obtained from this work are listed below.

1. By using GNSS TEC and taking a double-thin-shell approach, Es layer was observed only in the summer hemisphere when F-region conjugate structures simultaneously occur in both hemispheres; Es layers in the

summer hemisphere appear ~30 min earlier than the MSTIDs in the F region, and followed by the coupled E- and F-region disturbances, as well as the geomagnetic conjugate MSTIDs. These results support the evidence that the F-region conjugate irregularities in both hemispheres are mainly driven by the Es layers in the summer hemisphere during the interhemispheric coupling process.

2. The sporadic and blanketing E layers with small amplitudes in the winter hemisphere were observed to show intensity reduction or even dissipation after the interhemispheric coupling, which may be related to the variation in ionospheric conductivity caused by the thermospheric winds in the winter hemisphere and the conjugate MSTIDs (more importantly).
3. Thermospheric winds play an important role in the MSTID generation and development. In addition, the MSTID intensity decreases more rapidly in the winter hemisphere, which may be related to the decoupling from the summer hemisphere.
4. Thermospheric winds, non-equipotential magnetic field lines, and background TEC could be the factors that associate with the asymmetry in the amplitude of hemispheric conjugate MSTIDs and the slower growth rate of MSTID structures in the winter hemisphere.

Data Availability Statement

The GNSS data can be accessed at Geospatial Information Authority of Japan (GSI; https://www.gsi.go.jp/ENGLISH/geonet_english.html) and the Geoscience Australia GNSS data archive (https://www.ga.gov.au/scientific-topics/positioning-navigation/geodesy/gnss-networks/data-and-site-logs). The ionosonde data are provided by National Institute of Information and Communications Technology (NICT; https://wdc.nict.go.jp/IONO/) and the Space Weather Service Bureau of Meteorology Australia (https://www.sws.bom.gov.au/World_Data_Centre/1/1). ICON data can be retrieved from the ICON website (https://icon.ssl.berkeley.edu/Data). Swarm data are publicly accessible at ftp://swarm-diss.eo.esa.int. COSMIC data can be obtained from COSMIC Data Analysis and Archive Center (CDAAC) at https://www.cosmic.ucar.edu/. Fabry-Perot interferometer (FPI) data can be found at https://stdb2.isee.nagoya-u.ac.jp/omti/. K index data are provided by Kakioka magnetic observatory at http://www.kakioka-jma.go.jp/obsdata/obsdata.html.

Acknowledgments
This work was supported by JST SPRING Grant Number JPMJSP2110, and JSPS KAKENHI Grant Numbers JP21H04518 and JP22K21345.

References

Abdu, M., De Souza, J., Batista, I., Santos, A., Sobral, J., Rastogi, R., & Chandra, H. (2014). The role of electric fields in sporadic E layer formation over low latitudes under quiet and magnetic storm conditions. *Journal of Atmospheric and Solar-Terrestrial Physics*, *115*, 95–105. https://doi.org/10.1016/j.jastp.2013.12.003

Alken, P., Thébault, E., Beggan, C. D., Amit, H., Aubert, J., Baerenzung, J., et al. (2021). International geomagnetic reference field: The thirteenth generation. *Earth, Planets and Space*, *73*(1), 1–25. https://doi.org/10.1186/s40623-020-01288-x

Bowman, G. (1985). Some aspects of mid-latitude spread-Es, and its relationship with spread-F. *Planetary and Space Science*, *33*(9), 1081–1089. https://doi.org/10.1016/0032-0633(85)90027-3

Bowman, G. (1990). A review of some recent work on mid-latitude spread-F occurrence as detected by ionosondes. *Journal of Geomagnetism and Geoelectricity*, *42*(2), 109–138. https://doi.org/10.5636/jgg.42.109

Buonsanto, M., & Foster, J. (1993). Effects of magnetospheric electric fields and neutral winds on the low-middle latitude ionosphere during the March 20–21, 1990, storm. *Journal of Geophysical Research*, *98*(A11), 19133–19140. https://doi.org/10.1029/93JA01807

Buonsanto, M., Foster, J., Galasso, A., Sipler, D., & Holt, J. (1990). Neutral winds and thermosphere/ionosphere coupling and energetics during the geomagnetic disturbances of March 6–10, 1989. *Journal of Geophysical Research*, *95*(A12), 21033–21050. https://doi.org/10.1029/JA095iA12p21033

Burke, W., Martinis, C., Lai, P., Gentile, L., Sullivan, C., & Pfaff, R. F. (2016). C/NOFS observations of electromagnetic coupling between magnetically conjugate MSTID structures. *Journal of Geophysical Research: Space Physics*, *121*(3), 2569–2582. https://doi.org/10.1002/2015JA021965

Chen, J., Lei, J., Zhang, S., Wang, W., & Dang, T. (2020). A simulation study on the relationship between field-aligned and field-perpendicular plasma velocities in the ionospheric F region. *Journal of Geophysical Research: Space Physics*, *125*(1), e2019JA027350. https://doi.org/10.1029/2019JA027350

Cherniak, I., Zakharenkova, I., Braun, J., Wu, Q., Pedatella, N., Schreiner, W., et al. (2021). Accuracy assessment of the quiet-time ionospheric F2 peak parameters as derived from COSMIC-2 multi-GNSS radio occultation measurements. *Journal of Space Weather and Space Climate*, *11*, 18. https://doi.org/10.1051/swsc/2020080

Cosgrove, R. B. (2007). Generation of mesoscale F layer structure and electric fields by the combined Perkins and Es layer instabilities, in simulations. *Annales Geophysicae*, *25*(7), 1579–1601. https://doi.org/10.5194/angeo-25-1579-2007

Cosgrove, R. B. (2013). Mechanisms for E–F coupling and their manifestation. *Journal of Atmospheric and Solar-Terrestrial Physics*, *103*, 56–65. https://doi.org/10.1016/j.jastp.2013.03.011

Cosgrove, R. B., & Tsunoda, R. T. (2002). A direction-dependent instability of sporadic-E layers in the nighttime midlatitude ionosphere. *Geophysical Research Letters*, *29*(18), 11–1. https://doi.org/10.1029/2002GL014669

Cosgrove, R. B., & Tsunoda, R. T. (2004). Instability of the E-F coupled nighttime midlatitude ionosphere. *Journal of Geophysical Research*, *109*(A4), A04305. https://doi.org/10.1029/2003JA010243

Cosgrove, R. B., Tsunoda, R. T., Fukao, S., & Yamamoto, M. (2004). Coupling of the Perkins instability and the sporadic E layer instability derived from physical arguments. *Journal of Geophysical Research*, *109*(A6), A06301. https://doi.org/10.1029/2003JA010295

Ding, F., Wan, W., Xu, G., Yu, T., Yang, G., & Wang, J.-s. (2011). Climatology of medium-scale traveling ionospheric disturbances observed by a GPS network in central China. *Journal of Geophysical Research*, *116*(A9). https://doi.org/10.1029/2011JA016545

Farley, D., Jr. (1959). A theory of electrostatic fields in a horizontally stratified ionosphere subject to a vertical magnetic field. *Journal of Geophysical Research*, *64*(9), 1225–1233. https://doi.org/10.1029/JZ064i009p01225

Finlay, C. C., Kloss, C., Olsen, N., Hammer, M. D., Tøffner-Clausen, L., Grayver, A., & Kuvshinov, A. (2020). The CHAOS-7 geomagnetic field model and observed changes in the South Atlantic Anomaly. *Earth, Planets and Space*, *72*(1), 1–31. https://doi.org/10.1186/s40623-020-01252-9

Forbes, J. M., Bruinsma, S. L., Miyoshi, Y., & Fujiwara, H. (2008). A solar terminator wave in thermosphere neutral densities measured by the CHAMP satellite. *Geophysical Research Letters*, *35*(14), L14802. https://doi.org/10.1029/2008GL034075

Fu, W., Ma, G., Lu, W., Maruyama, T., Li, J., Wan, Q., et al. (2021). Improvement of global ionospheric TEC derivation with multi-source data in modip latitude. *Atmosphere*, *12*(4), 434. https://doi.org/10.3390/atmos12040434

Fu, W., Ssessanga, N., Yokoyama, T., & Yamamoto, M. (2021). High-resolution 3-D imaging of daytime sporadic-E over Japan by using GNSS TEC and ionosondes. *Space Weather*, *19*(12), e2021SW002878. https://doi.org/10.1029/2021SW002878

Fu, W., Yokoyama, T., Ssessanga, N., Yamamoto, M., & Liu, P. (2022). On using a double-thin-shell approach and TEC perturbation component to sound night-time mid-latitude E–F coupling. *Earth, Planets and Space*, *74*(1), 1–17. https://doi.org/10.1186/s40623-022-01639-w

Haldoupis, C. (2012). Midlatitude sporadic E. A typical paradigm of atmosphere-ionosphere coupling. *Space Science Reviews*, *168*(1), 441–461. https://doi.org/10.1007/s11214-011-9786-8

Haldoupis, C., Kelley, M. C., Hussey, G. C., & Shalimov, S. (2003). Role of unstable sporadic-E layers in the generation of midlatitude spread F. *Journal of Geophysical Research*, *108*(A12), 1446. https://doi.org/10.1029/2003JA009956

Haldoupis, C., Pancheva, D., Singer, W., Meek, C., & MacDougall, J. (2007). An explanation for the seasonal dependence of midlatitude sporadic E layers. *Journal of Geophysical Research*, *112*(A6). https://doi.org/10.1029/2007JA012322

Harding, B. J., Chau, J. L., He, M., Englert, C. R., Harlander, J. M., Marr, K. D., et al. (2021). Validation of ICON-MIGHTI thermospheric wind observations: 2. Green-line comparisons to specular meteor radars. *Journal of Geophysical Research: Space Physics*, *126*(3), e2020JA028947. https://doi.org/10.1029/2020JA028947

Harding, B. J., Wu, Y.-J. J., Alken, P., Yamazaki, Y., Triplett, C. C., Immel, T. J., et al. (2022). Impacts of the January 2022 Tonga volcanic eruption on the ionospheric dynamo: ICON-MIGHTI and swarm observations of extreme neutral winds and currents. *Geophysical Research Letters*, *49*(9), e2022GL098577. https://doi.org/10.1029/2022GL098577

He, M., Liu, L., Wan, W., & Zhao, B. (2011). A study on the nighttime midlatitude ionospheric trough. *Journal of Geophysical Research*, *116*(A5). https://doi.org/10.1029/2010JA016252

Heelis, R., Crowley, G., Rodrigues, F., Reynolds, A., Wilder, R., Azeem, I., & Maute, A. (2012). The role of zonal winds in the production of a pre-reversal enhancement in the vertical ion drift in the low latitude ionosphere. *Journal of Geophysical Research*, *117*(A8). https://doi.org/10.1029/2012JA017547

Hooke, W. H. (1968). Ionospheric irregularities produced by internal atmospheric gravity waves. *Journal of Atmospheric and Terrestrial Physics*, *30*(5), 795–823. https://doi.org/10.1016/S0021-9169(68)80033-9

Hunsucker, R. D. (1982). Atmospheric gravity waves generated in the high-latitude ionosphere: A review. *Reviews of Geophysics*, *20*(2), 293–315. https://doi.org/10.1029/RG020i002p00293

Kelley, M. C. (2009). *The Earth's ionosphere: Plasma physics and electrodynamics*. Academic Press.

Kil, H., & Paxton, L. J. (2017). Global distribution of nighttime medium-scale traveling ionospheric disturbances seen by swarm satellites. *Geophysical Research Letters*, *44*(18), 9176–9182. https://doi.org/10.1002/2017GL074750

Larsen, M. (2002). Winds and shears in the mesosphere and lower thermosphere: Results from four decades of chemical release wind measurements. *Journal of Geophysical Research*, *107*(A8), SIA28-1–SIA28-14. https://doi.org/10.1029/2001JA000218

Lee, W. K., Kil, H., & Paxton, L. J. (2021). Global distribution of nighttime MSTIDs and its association with E region irregularities seen by CHAMP satellite. *Journal of Geophysical Research: Space Physics*, *126*(5), e2020JA028836. https://doi.org/10.1029/2020JA028836

Lin, C.-Y., Lin, C. C.-H., Liu, J.-Y., Rajesh, P., Matsuo, T., Chou, M.-Y., et al. (2020). The early results and validation of FORMOSAT-7/COSMIC-2 space weather products: Global ionospheric specification and Ne-aided Abel electron density profile. *Journal of Geophysical Research: Space Physics*, *125*(10), e2020JA028028. https://doi.org/10.1029/2020JA028028

Liu, Y., Zhou, C., Tang, Q., Kong, J., Gu, X., Ni, B., et al. (2019). Evidence of mid-and low-latitude nighttime ionospheric *E–F* coupling: Coordinated observations of sporadic *E* layers, *F*-region field-aligned irregularities, and medium-scale traveling ionospheric disturbances. *IEEE Transactions on Geoscience and Remote Sensing*, *57*(10), 7547–7557. https://doi.org/10.1109/TGRS.2019.2914059

Liu, Y., Zhou, C., Xu, T., Wang, Z., Tang, Q., Deng, Z., & Chen, G. (2020). Investigation of midlatitude nighttime ionospheric E-F coupling and interhemispheric coupling by using cosmic GPS radio occultation measurements. *Journal of Geophysical Research: Space Physics*, *125*(3), e2019JA027625. https://doi.org/10.1029/2019JA027625

Lühr, H., Rother, M., Maus, S., Mai, W., & Cooke, D. (2003). The diamagnetic effect of the equatorial Appleton anomaly: Its characteristics and impact on geomagnetic field modeling. *Geophysical Research Letters*, *30*(17). https://doi.org/10.1029/2003GL017407

Ma, G., Gao, W., Li, J., Chen, Y., & Shen, H. (2014). Estimation of GPS instrumental biases from small scale network. *Advances in Space Research*, *54*(5), 871–882. https://doi.org/10.1016/j.asr.2013.01.008

Ma, G., & Maruyama, T. (2003). Derivation of TEC and estimation of instrumental biases from GEONET in Japan. *Annales Geophysicae*, *21*(10), 2083–2093. https://doi.org/10.5194/angeo-21-2083-2003

Maeda, J., & Heki, K. (2014). Two-dimensional observations of midlatitude sporadic E irregularities with a dense GPS array in Japan. *Radio Science*, *49*(1), 28–35. https://doi.org/10.1002/2013RS005295

Maeda, J., & Heki, K. (2015). Morphology and dynamics of daytime mid-latitude sporadic-E patches revealed by GPS total electron content observations in Japan. *Earth, Planets and Space*, *67*(1), 1–9. https://doi.org/10.1186/s40623-015-0257-4

Makela, J. J., Baughman, M., Navarro, L. A., Harding, B. J., Englert, C. R., Harlander, J. M., et al. (2021). Validation of ICON-MIGHTI thermospheric wind observations: 1. Nighttime red-line ground-based Fabry-Perot interferometers. *Journal of Geophysical Research: Space Physics*, *126*(2), e2020JA028726. https://doi.org/10.1029/2020JA028726

Maruyama, T., Saito, S., Yamamoto, M., & Fukao, S. (2006). Simultaneous observation of sporadic E with a rapid-run ionosonde and VHF coherent backscatter radar. *Annales Geophysicae*, *24*(1), 153–162. https://doi.org/10.5194/angeo-24-153-2006

Mathews, J. (1998). Sporadic E: Current views and recent progress. *Journal of Atmospheric and Solar-Terrestrial Physics*, *60*(4), 413–435. https://doi.org/10.1016/S1364-6826(97)00043-6

Miyoshi, Y., Fujiwara, H., Forbes, J. M., & Bruinsma, S. L. (2009). Solar terminator wave and its relation to the atmospheric tide. *Journal of Geophysical Research*, *114*(A7). https://doi.org/10.1029/2009JA014110

Narayanan, V., Shiokawa, K., Otsuka, Y., & Neudegg, D. (2018). On the role of thermospheric winds and sporadic E layers in the formation and evolution of electrified MSTIDs in geomagnetic conjugate regions. *Journal of Geophysical Research: Space Physics*, *123*(8), 6957–6980. https://doi.org/10.1029/2018JA025261

Olsen, N., Hulot, G., Lesur, V., Finlay, C. C., Beggan, C., Chulliat, A., et al. (2015). The Swarm initial field model for the 2014 geomagnetic field. *Geophysical Research Letters*, *42*(4), 1092–1098. https://doi.org/10.1002/2014GL062659

Otsuka, Y. (2021). Medium-scale traveling ionospheric disturbances. *Ionosphere Dynamics and Applications*, 421–437. https://doi.org/10.1002/9781119815617.ch18

Otsuka, Y., Onoma, F., Shiokawa, K., Ogawa, T., Yamamoto, M., & Fukao, S. (2007). Simultaneous observations of nighttime medium-scale traveling ionospheric disturbances and E region field-aligned irregularities at midlatitude. *Journal of Geophysical Research*, *112*(A6). https://doi.org/10.1029/2005JA011548

Otsuka, Y., Shinbori, A., Tsugawa, T., & Nishioka, M. (2021). Solar activity dependence of medium-scale traveling ionospheric disturbances using GPS receivers in Japan. *Earth, Planets and Space*, *73*(1), 1–11. https://doi.org/10.1186/s40623-020-01353-5

Otsuka, Y., Shiokawa, K., Ogawa, T., & Wilkinson, P. (2004). Geomagnetic conjugate observations of medium-scale traveling ionospheric disturbances at midlatitude using all-sky airglow imagers. *Geophysical Research Letters*, *31*(15), L15803. https://doi.org/10.1029/2004GL020262

Otsuka, Y., Suzuki, K., Nakagawa, S., Nishioka, M., Shiokawa, K., & Tsugawa, a. (2013). GPS observations of medium-scale traveling ionospheric disturbances over Europe. *Annales Geophysicae*, *31*(2), 163–172. https://doi.org/10.5194/angeo-31-163-2013

Otsuka, Y., Tani, T., Tsugawa, T., Ogawa, T., & Saito, A. (2008). Statistical study of relationship between medium-scale traveling ionospheric disturbance and sporadic E layer activities in summer night over Japan. *Journal of Atmospheric and Solar-Terrestrial Physics*, *70*(17), 2196–2202. https://doi.org/10.1016/j.jastp.2008.07.008

Park, J., Lühr, H., Kervalishvili, G., Rauberg, J., Michaelis, I., Stolle, C., & Kwak, Y.-S. (2015). Nighttime magnetic field fluctuations in the topside ionosphere at midlatitudes and their relation to medium-scale traveling ionospheric disturbances: The spatial structure and scale sizes. *Journal of Geophysical Research: Space Physics*, *120*(8), 6818–6830. https://doi.org/10.1002/2015JA021315

Park, J., Lühr, H., Stolle, C., Rother, M., Min, K. W., Chung, J.-K., et al. (2009a). Magnetic signatures of medium-scale traveling ionospheric disturbances as observed by CHAMP. *Journal of Geophysical Research*, *114*(A3). https://doi.org/10.1029/2008JA013792

Park, J., Lühr, H., Stolle, C., Rother, M., Min, K., & Michaelis, I. (2009b). The characteristics of field-aligned currents associated with equatorial plasma bubbles as observed by the CHAMP satellite. *Annales Geophysicae*, *27*(7), 2685–2697. https://doi.org/10.5194/angeo-27-2685-2009

Perkins, F. (1973). Spread F and ionospheric currents. *Journal of Geophysical Research*, *78*(1), 218–226. https://doi.org/10.1029/JA078i001p00218

Pitteway, M., & Hines, C. (1963). The viscous damping of atmospheric gravity waves. *Canadian Journal of Physics*, *41*(12), 1935–1948. https://doi.org/10.1139/p63-194

Saito, A., Fukao, S., & Miyazaki, S. (1998). High resolution mapping of TEC perturbations with the GSI GPS network over Japan. *Geophysical Research Letters*, *25*(16), 3079–3082. https://doi.org/10.1029/98GL52361

Saito, A., Iyemori, T., Blomberg, L., Yamamoto, M., & Takeda, M. (1998). Conjugate observations of the mid-latitude electric field fluctuations with the MU radar and the Freja satellite. *Journal of Atmospheric and Solar-Terrestrial Physics*, *60*(1), 129–140. https://doi.org/10.1016/S1364-6826(97)00094-1

Saito, A., Nishimura, M., Yamamoto, M., Fukao, S., Kubota, M., Shiokawa, K., et al. (2001). Traveling ionospheric disturbances detected in the FRONT campaign. *Geophysical Research Letters*, *28*(4), 689–692. https://doi.org/10.1029/2000GL011884

Saito, S., Yamamoto, M., Hashiguchi, H., Maegawa, A., & Saito, A. (2007). Observational evidence of coupling between quasi-periodic echoes and medium scale traveling ionospheric disturbances. *Annales Geophysicae*, *25*(10), 2185–2194. https://doi.org/10.5194/angeo-25-2185-2007

Shiokawa, K., Ihara, C., Otsuka, Y., & Ogawa, T. (2003). Statistical study of nighttime medium-scale traveling ionospheric disturbances using midlatitude airglow images. *Journal of Geophysical Research*, *108*(A1), 1052. https://doi.org/10.1029/2002JA009491

Shiokawa, K., Otsuka, Y., Ihara, C., Ogawa, T., & Rich, F. (2003). Ground and satellite observations of nighttime medium-scale traveling ionospheric disturbance at midlatitude. *Journal of Geophysical Research*, *108*(A4), 1145. https://doi.org/10.1029/2002JA009639

Shiokawa, K., Otsuka, Y., Tsugawa, T., Ogawa, T., Saito, A., Ohshima, K., et al. (2005). Geomagnetic conjugate observation of nighttime medium-scale and large-scale traveling ionospheric disturbances: FRONT3 campaign. *Journal of Geophysical Research*, *110*(A5). A05303. https://doi.org/10.1029/2004JA010845

Sinno, K., Ouchi, C., & Nemoto, C. (1964). Structure and movement of Es detected by LORAN observations. *Journal of Geomagnetism and Geoelectricity*, *16*(2), 75–88. https://doi.org/10.5636/jgg.16.75

Somsikov, V. (2011). Solar terminator and dynamic phenomena in the atmosphere: A review. *Geomagnetism and Aeronomy*, *51*(6), 707–719. https://doi.org/10.1134/S0016793211060168

Ssessanga, N., Kim, Y. H., & Kim, E. (2015). Vertical structure of medium-scale traveling ionospheric disturbances. *Geophysical Research Letters*, *42*(21), 9156–9165. https://doi.org/10.1002/2015GL066093

Tepley, C., Robles, E., García, R., Santos, P., Brum, C., & Burnside, R. (2011). Directional trends in thermospheric neutral winds observed at Arecibo during the past three solar cycles. *Journal of Geophysical Research*, *116*(A2). https://doi.org/10.1029/2010JA016172

Tsugawa, T., Nishioka, M., Ishii, M., Hozumi, K., Saito, S., Shinbori, A., et al. (2018). Total electron content observations by dense regional and worldwide international networks of GNSS. *Journal of Disaster Research*, *13*(3), 535–545. https://doi.org/10.20965/jdr.2018.p0535

Tsunoda, R. T. (2006). On the coupling of layer instabilities in the nighttime midlatitude ionosphere. *Journal of Geophysical Research*, *111*(A11), A11304. https://doi.org/10.1029/2006JA011630

Tsunoda, R. T., & Cosgrove, R. B. (2001). Coupled electrodynamics in the nighttime midlatitude ionosphere. *Geophysical Research Letters*, *28*(22), 4171–4174. https://doi.org/10.1029/2001GL013245

Valladares, C. E., & Sheehan, R. (2016). Observations of conjugate MSTIDs using networks of GPS receivers in the American sector. *Radio Science*, *51*(9), 1470–1488. https://doi.org/10.1002/2016RS005967

Wan, X., Xiong, C., Wang, H., Zhang, K., & Yin, F. (2020). Spatial characteristics on the occurrence of the nighttime midlatitude medium-scale traveling ionospheric disturbance at topside ionosphere revealed by the Swarm satellite. *Journal of Geophysical Research: Space Physics*, *125*(8), e2019JA027739. https://doi.org/10.1029/2019JA027739

Whitehead, J. (1989). Recent work on mid-latitude and equatorial sporadic-E. *Journal of Atmospheric and Terrestrial Physics*, *51*(5), 401–424. https://doi.org/10.1016/0021-9169(89)90122-0

Wu, D. L., Ao, C. O., Hajj, G. A., de La Torre Juarez, M., & Mannucci, A. J. (2005). Sporadic E morphology from GPS-CHAMP radio occultation. *Journal of Geophysical Research*, *110*(A1), A01306. https://doi.org/10.1029/2004JA010701

Yokoyama, T. (2014). Hemisphere-coupled modeling of nighttime medium-scale traveling ionospheric disturbances. *Advances in Space Research*, *54*(3), 481–488. https://doi.org/10.1016/j.asr.2013.07.048

Yokoyama, T., & Hysell, D. L. (2010). A new midlatitude ionosphere electrodynamics coupling model (MIECO): Latitudinal dependence and propagation of medium-scale traveling ionospheric disturbances. *Geophysical Research Letters*, *37*(8). https://doi.org/10.1029/2010GL042598

Yokoyama, T., Hysell, D. L., Otsuka, Y., & Yamamoto, M. (2009). Three-dimensional simulation of the coupled Perkins and Es-layer instabilities in the nighttime midlatitude ionosphere. *Journal of Geophysical Research*, *114*(A3). https://doi.org/10.1029/2008JA013789

Yokoyama, T., Jin, H., & Shinagawa, H. (2015). West wall structuring of equatorial plasma bubbles simulated by three-dimensional HIRB model. *Journal of Geophysical Research: Space Physics*, *120*(10), 8810–8816. https://doi.org/10.1002/2015JA021799

Yokoyama, T., & Stolle, C. (2017). Low and midlatitude ionospheric plasma density irregularities and their effects on geomagnetic field. *Space Science Reviews*, *206*(1), 495–519. https://doi.org/10.1007/s11214-016-0295-7

Yokoyama, T., Yamamoto, M., Fukao, S., & Cosgrove, R. (2004). Three-dimensional simulation on generation of polarization electric field in the midlatitude E-region ionosphere. *Journal of Geophysical Research*, *109*(A1), A01309. https://doi.org/10.1029/2003JA010238

Yokoyama, T., Yamamoto, M., Fukao, S., Takahashi, T., & Tanaka, M. (2005). Numerical simulation of mid-latitude ionospheric E-region based on SEEK and SEEK-2 observations. *Annales Geophysicae*, *23*(7), 2377–2384. https://doi.org/10.5194/angeo-23-2377-2005